Chapter 9
Perovskite Material-Based Photocatalysts

Ravi Gundeboina, Venkataswamy Perala and Vithal Muga

1 Introduction

The rapid industrialization, the progression of human civilization, and escalating the use of traditional fossil fuels ensued in the extreme limits of pollution of air, water, and soil. It is observed that over the past few decades, the abusive use of pesticides, industrial chemicals, pharmaceutical and personal care products (PPCPs), organic dyes, and combustion byproducts have resulted in their undesirable accumulation in the environment. Of these, organic dyes have been extensively used in industries such as fabric, furniture, food, and paint. It is estimated that about 30–40% of these coloring agents in the form of "dye wastewater" are released (accidentally or without pretreatment) into water streams causing environmental and health problems. A few of these water-soluble dyes prevent sunlight causing damage to aquatic life. Some other dyes on exposure to sunlight decompose and generate carcinogenic byproducts. The mounting level of pollution together with the depletion of fossil fuel has forced scientists to look for new alternative energy sources and more effective mechanisms to curb pollution. Thus, the utilization of solar energy through a sustainable and cost-effective approach offers the solution to (a) reduce environmental pollution and (b) satisfy the demand for renewable energy.

Traditional methods of wastewater treatment such as coagulation, microbial degradation, adsorption of activated carbon, incineration, filtration, and sedimentation have become ineffective from an economic point of view or leave secondary pollutants. Advanced oxidation processes (AOPs), a group of established treatment methods including (i) photocatalytic oxidation using a semiconducting material as catalyst, (ii) ultrasonic cavitation, (iii) electron beam irradiation, (iv) Fenton's

R. Gundeboina · V. Perala · V. Muga (✉)
Department of Chemistry, Osmania University, Hyderabad 500 007, Telangana, India
e-mail: mugavithal@rediffmail.com

N. S. Arul and V. D. Nithya (eds.), *Revolution of Perovskite*, Materials Horizons: From Nature to Nanomaterials, https://doi.org/10.1007/978-981-15-1267-4_9

reaction, and (v) reactions using O_3/H_2O_2, UV/O_3, and UV/H_2O_2 are found to be effective. The principle of AOP is to generate robust oxidizing species such as OH radicals in situ, which initiates a series of reactions that break down the dye molecule into smaller and less harmful substances, the so-called mineralization process [1–3]. Despite the good oxidation of organic pollutants (except method (i)), the complexity of these methods (AOPs), the high chemical consumption, and the relatively high treatment costs constitute the significant barriers for large-scale applications [2]. Hence, semiconducting material as a photocatalyst is anticipated to be both supplementary and complementary to a more conventional approach for the devastation of dangerous chemical wastes and energy production.

1.1 Heterogeneous Photocatalysis—Semiconductor Oxides as Photocatalysts

The execution of a chemical or biochemical reaction on the surface of the inorganic semiconductor is referred to as heterogeneous photocatalysis. For the fundamentals of photocatalysis, the readers can go through the excellent reviews reported [4–9]. The catalyst together with reactants/pollutants, upon irradiation of light, produce an electron (in conduction band) and hole (in valence band) leading to a series of reactions in which useful products are formed, or undesirable pollutants are decomposed to less harmful byproducts. The phase pure, well-crystallized, monodisperse, nano-sized semiconductor oxide with homogeneous morphology is ideal to be an efficient and chemically stable photocatalyst. As the abovementioned properties strongly depend on the preparative conditions of material, the selection of preparation method is essential. It is well known that the efficiency of a photocatalytic reaction or photocatalyst depends on several factors such as its crystallite size, surface area, band gap energy (E_g), recombination rate of photogenerated electron–hole pair during the photoreaction, nature of the reactant/pollutant, and nature of active sites on the catalyst, to mention a few (Fig. 1) [10]. The photocatalyst used must satisfy several functional requirements with respect to semiconducting properties: (i) suitable solar visible light absorption capacity with a band gap energy about 2.0–2.2 eV (visible light region) and band edge potentials suitable for splitting of water, (ii) capability for separating photoexcited electrons from reactive holes, (iii) minimization of energy losses related to charge transport and recombination of photoexcited electron–hole pair, (iv) chemical stability against corrosion and photo-corrosion in aqueous environment, (v) kinetically sui electron transfer properties from photocatalytic surface of water, and (vi) easy and cost-effective method of preparation.

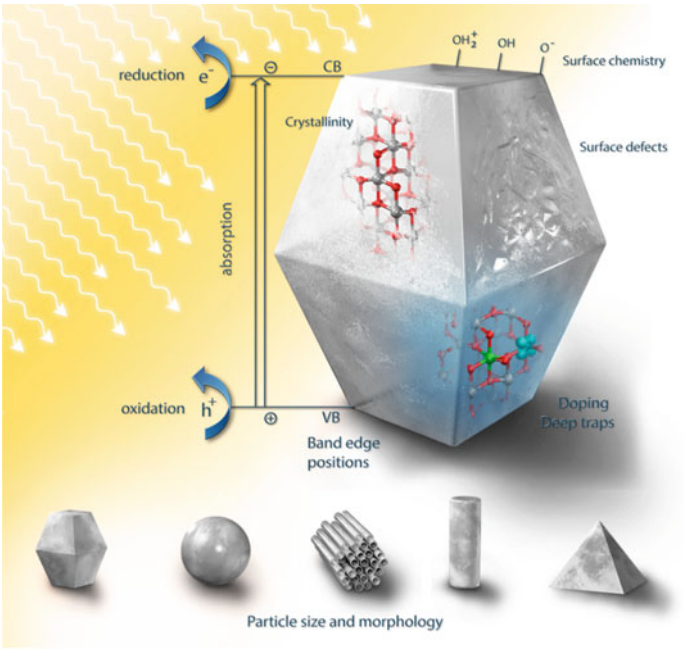

Fig. 1 Factors impacting photocatalytic activity of a single (idealized) inorganic semiconductor particle [10] Copyright 2018. Reprinted with permission from ACS publications

1.2 Mechanism of Semiconductor Photocatalysis

When a semiconductor absorbs light energy more than its band gap energy, it results in the promotion of the valence band electron into its conduction band. The formation of the electron (in the conduction band) and hole (in the valence band), known as "exciton" is the first step in the mechanism of semiconductor photocatalysis.

$$\text{Photocatalyst(PC)} + h\upsilon \rightarrow \text{PC}\left(h_{\text{VB}}^{+} + e_{\text{CB}}^{-}\right)$$

After photoexcitation, the excited electron–hole pairs either recombine or can migrate to the surface of the semiconductor. They (electron and hole) participate in various oxidation and reduction reactions with adsorbed species such as H_2O and O_2. These oxidation and reductions are the primary reactions of photocatalytic degradation of pollutants and photocatalytic hydrogen production, respectively. In the photocatalytic water splitting reactions, the photoexcited electrons in the conduction band (CB) are responsible for generation of H_2 and OH^- by reacting with water. However, in order to initiate hydrogen and oxygen production, the conduction band level of the semiconductor should be more negative than the reduction potential of H_2 (H^+/H_2) and valence band level should be more positive than the

oxidation potential of O_2 (H_2O/O_2). However, the photocatalytic dye degradation mechanism is strongly affected by different model pollutants and photocatalysts. In addition, the different dominant radical species would determine the photoactivity and the decomposition path. Hence, the dye degradation mechanism is still not fully understood, even uncertain. A basic mechanism for the photocatalytic process of a semiconductor dye degradation and water splitting is presented in Figs. 2 and 3, respectively.

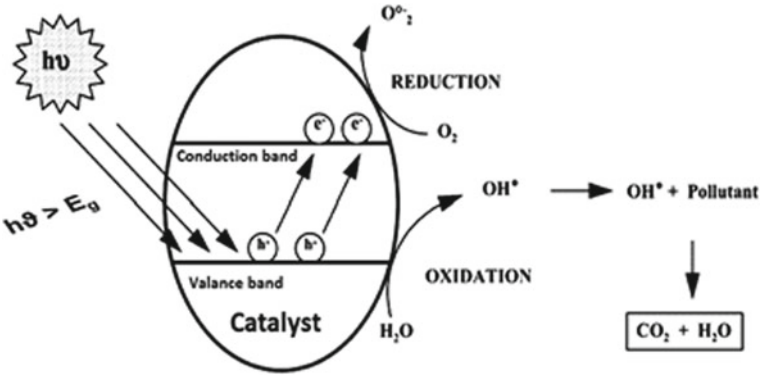

Fig. 2 Degradation process of pollutants using semiconductor oxides illuminated by UV light/ solar light

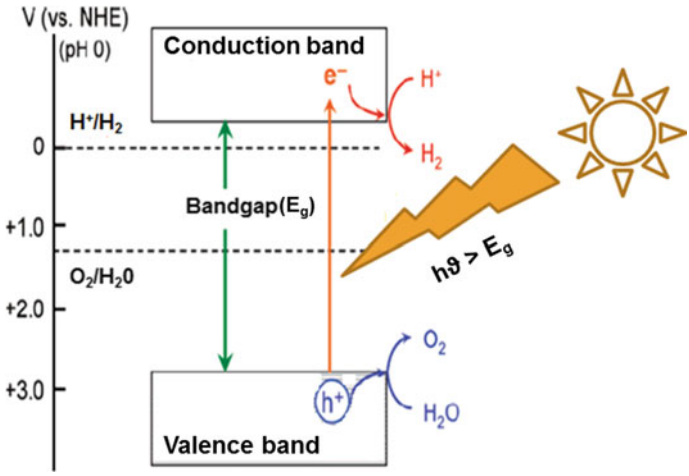

Fig. 3 Fundamental principle of semiconductor-based photocatalytic water splitting for hydrogen and oxygen production

2 Methods to Tailor the Photocatalytic Properties of Semiconductor Photocatalysts

Since the discovery of Fujishima and Honda [11] that water can be photo-electrochemically decomposed into H_2 and O_2 using a semiconductor (TiO_2) electrode under UV irradiation, extensive works have been carried out to produce hydrogen from water splitting using a variety of semiconductor photocatalysts. Since the major part (about 45%) of sunlight belongs to visible region, it is essential that the efforts to design the semiconducting photocatalysts should be toward the utilization of this part of solar light to ignite photocatalytic reactions. Hence, control of electronic band structure of material by adjusting its elemental compositions was recognized as the effective method to extend light response range.

The methods including metal and nonmetal substitution into semiconductor materials are considered to tailor its wide band gap to narrow band gap. Metal ion substitution creates impurity levels in the forbidden band as either a donor level above the valence band or an acceptor level below the conduction band as shown in Fig. 4.

These impurity energy levels decrease the band gap energy of the photocatalyst, thus shifting the photo-response of catalyst toward the visible region. There have been numerous reports on the modification of wide band gap photocatalysts using metal ion doping to make them visible light active [12–17].

It is also perceived in some cases that metal ion dopant can also act as a recombination center, resulting in decreased photocatalytic activities [12]. Doping of nonmetal ions such as N^{3-}, S^{2-}, and F^{-} is another method employed to narrow the band gap and improve the photocatalytic activity. Unlike metal ion dopants, nonmetal ion dopants are less likely to form donor levels in the forbidden band and

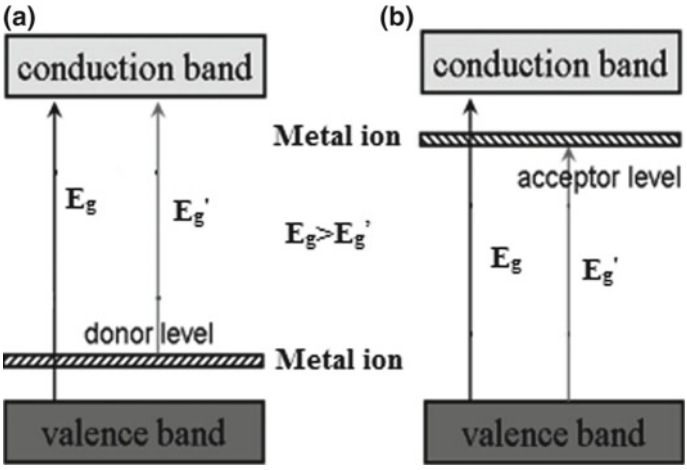

Fig. 4 **a** Donor level and **b** acceptor level formed by metal ion doping

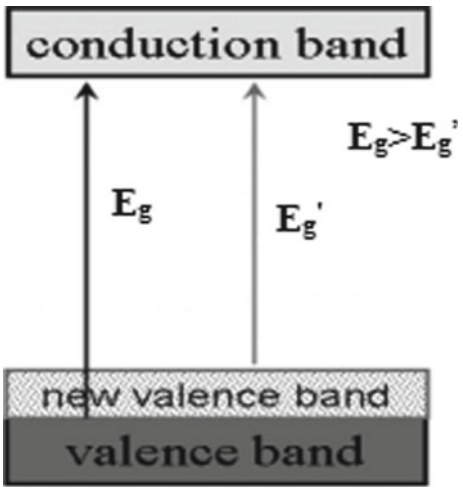

Fig. 5 New valence band formation by doping of nonmetal ions

recombination centers. Hence, anion doping is more effective to enhance the photocatalytic activity. Since the study of N-doped TiO_2 by Asahi et al., the photocatalytic studies of anion-doped semiconductors have been attracted much attention. It was found that N substitution into the metal oxide can shift its photo-response into the visible region because of the contribution of N *2p* orbitals to the valence band comprised of O *2p* orbitals, thereby narrowing the band gap by moving the valence band upward (Fig. 5) [18]. The method of nonmetal ion doping has been widely used to modify some UV-light-active oxide photocatalysts [19–24].

However, there are also two momentous drawbacks observed in visible light-responsive photocatalytic reactions. First is the rapid recombination of electron/hole (e^-/h^+) pair. The second is low utilization of visible-light-excited high-level energy electrons (HLEEs) and limited visible light absorption of semiconductor photocatalyst. Moreover, there is an additional problem of rapid backward reaction during water splitting. These drawbacks can be overcome by the development of novel photocatalysts such as metal/nonmetal doped photocatalyst, noble metal surface-modified photocatalyst [25–27], dye/semiconductor-sensitized photocatalyst, and p–n heterojunction structure composite photocatalyst [28, 29].

The dopant in lattice brings defects and tunes the amount of oxygen vacancy. It is known that the photocatalyst, having lattice defects and oxygen vacancies, shows good photocatalytic properties by narrowing the band gap and suppressing recombination rate of photogenerated electron–hole [30–32]. When the noble metal is loaded onto the surface of the photocatalyst, the photogenerated electrons migrate to the surface of the host photocatalyst and are entrapped by the noble metal cocatalyst. Meanwhile, the photogenerated holes stay at the host photocatalyst and migrate to its surface. This results in the efficient separation of the photogenerated electrons and holes. Subsequently, the separately localized electrons and holes become involved in their roles as the reducer and oxidizer, respectively, in the photocatalytic reaction. The noble metals, such as Pt, Au, Ru, Pd, Ag, and Rh, are

usually used as effective cocatalysts for photocatalytic water splitting. To date, Pt-loaded photocatalysts have the highest photocatalytic activity for hydrogen evolution from water splitting reaction under the visible light irradiation [33, 34].

The methods including sensitization with organic dyes, the coupling of either p-type and n-type semiconductor or small and large band gap semiconductors, are another ways to improve the photocatalytic properties [35–37]. In the dye-sensitized semiconductor photocatalysis, the dye molecule electrons excited by visible light can be injected into the conduction band of the semiconductor to initiate the catalytic reactions. In the composite photocatalyst (coupling of large band gap semiconductor with a small band gap semiconductor with a more negative conduction level), the excited electrons from conduction band of a small band gap semiconductor by the absorption of visible light can be injected into the conduction band of a large band gap semiconductor, while the photogenerated holes are trapped in a small band gap semiconductor. Thus, an effective electron–hole separation can be achieved by these methods and results in higher photocatalytic activity. However, in p–n heterojunction photocatalysis, because of the difference of band gap and position between the two different semiconductors, the strong internal electric field at the interface can initiate the transfer of photoinduced electrons to the conduction band (CB) of the n-type semiconductor and of holes to the valence band (VB) of the p-type semiconductor for the reduction and oxidation reactions, respectively [38, 39]. It has been observed that the visible-light-excited high-level energy electrons (HLEEs) of narrow band gap semiconductors such as Fe_2O_3, $BiVO_4$, and $BiFeO_3$ could transfer thermodynamically to the conduction band of TiO_2 with a high-energy level platform, leading to the extended lifetime of photogenerated charge carriers and hence to the improved visible light activities [40–42]. Recently, graphitic carbon nitride (g–C_3N_4) has been used as a kind of metal-free n-type semiconductor for enhancing the photocatalytic performance of materials with poor photocatalytic activity due to its unique advantages of hydrophilicity and large specific surface area [43].

3 A Short Overview of Perovskite Oxides as Photocatalysts

Among the various types of photocatalysts reported so far, the lion's share comes from oxide semiconductors. The ease of preparation, less expensive, less toxicity, possessing tunable properties, and their utility in cyclic experiments are some of the useful features that have made to investigate oxide semiconductors extensively compared to other types of materials. Oxides such as TiO_2, ZnO, WO_3, vanadates (VO_4), and molybdates have been considerably studied as photocatalysts. Oxides belonging to perovskite family with the general formula ABO_3 have attracted the scientific community due to their remarkable properties and the wide range of applications, interesting structure, and flexible compositions. The properties include

high chemical stability, catalytic properties [44], multiferroicity behavior [45], order/disorder transformations, and range of electrical and ionic conductivities that include metallic, half-metallic with spin-polarized electrical conductivity [46, 47], and superconductivity [48]. These oxides are used in SOFC technology, radioactive waste encapsulation, magnetic memory components, and dielectric resonator materials [47, 49–51]. These perovskite materials have a distinctive structural feature that is beneficial to photocatalytic activity. The relationship between crystal structure and energy delocalization shows that the closer to 180° the B–O–B bond angle is, the easier the excitation energy is delocalized leading to higher photoactivity [52, 53]. Thus, materials belonging to ABO_3 family with ideal perovskite structure are expected to exhibit higher photoactivity.

Perovskite oxides (ABO_3) with the structural flexibility to tolerate replacement of A- and B-sites with different ionic species have led to many novel compositions. This chapter exclusively deals with the research work published on the photocatalytic activity of ABO_3-based perovskite-type materials. Double, triple, and layered perovskites are not considered. Recently, there are fascinating review papers on perovskite materials related to their structure, synthesis, and applications in various fields. Ewelina Grabowska, reviewed the synthesis, characterization of selected perovskite oxides such as $SrTiO_3$, $KTaO_3$, $NaTaO_3$, $KNbO_3$, and $NaNbO_3$ and their applications in photocatalysis. Besides, the methods for enhancing the photocatalytic activity of those mentioned oxides along with the influence of different morphologies and surface properties are also discussed [54]. Guan et al. summarized the contemporary progress of perovskite materials and their photocatalytic applications in water splitting and environmental remediation, and presented the key challenges and viewpoints on the research of perovskite photocatalysts [55]. A review on photocatalytic CO_2 reduction using nano-sized perovskite oxides is reported by Sheng et al. This review correlated the physicochemical properties such as crystal structures, defect distribution, morphologies, and electronic properties to CO_2 photoreduction performance [56]. Pushkar Kanhere and Zhong Chen reviewed the perovskite materials that are classified by the B-site cations and their crystal structure, optical properties, and electronic structure accompanied by photocatalytic performance [57]. Saumyaprava et al. discussed the recent development of perovskite, layered perovskite, and their composites especially with π-conjugated carbon materials toward photocatalytic applications [58]. ABO_3-based photocatalysts for water splitting and the application of the modification scheme of ABO_3 photocatalysts in designing $A_xB_yO_z$ photocatalysts are systematically reviewed by Jinwen Shi and Liejin Guo [59]. Wei et al. described the basic principles of water splitting reaction, photodegradation of organic dyes and solar cells as well as the requirements for efficient photocatalysts [60]. Zhu et al. reviewed the catalytic performance of perovskite oxides with different morphologies for gas-, solid-, and liquid-phase reactions [61]. Shi et al. published a review on recent progress in photocatalytic CO_2 reduction over perovskite oxides. In this review, they have discussed recent advances in the design of perovskite oxides and their derivatives for photocatalytic CO_2 reduction, placing particular emphasis on structure

modulation, defect engineering, and interface construction as rational approaches for enhancing solar-driven CO_2 conversion to CH_4, CO, and other valuable oxygenates ($C_xH_yO_z$) [62].

4 Recent Developments in Enhancing the Photocatalytic Activity of Perovskite Materials

Although there are some review papers on the photocatalytic applications with simple ABO_3-based perovskite materials, a planned update is highly desirable to inform the latest progress, growing trends and updated summary of the current status concerning photocatalysis. Further, the rapid utilization of ABO_3 materials in photocatalytic applications requires a fresh assessment to provide a broad overview and possible future directions. Here, we have presented a review on the photocatalytic activity of lanthanum-based perovskites $LaMO_3$ (M = Fe, Co and Mn) and $BaMO_3$ (M = Zr and Sn) along with the recent developments in enhancing the photocatalytic behavior of alkali and alkaline earth metal-based perovskite materials ($ATiO_3$ (A = Ca, Ba, and Sr), $ATaO_3$ (A = Na and K), and $ANbO_3$ (A = Na and K)).

A succession of stable lanthanum-based perovskites, $LaMO_3$ (M = 3d transition metal) has been experimentally and theoretically expounded to be competent photocatalysts due to the unique crystal structure, electric conductivity, etc. Among these, $LaFeO_3$ has attracted a great deal of interest due to its narrow band gap, inimitable optoelectronic properties structural flexibility, and applications in removing the potential environmental pollutants. The photocatalytic performance of $LaFeO_3$ is low in spite of its narrow band gap energy ((2.1 eV (for dense polycrystalline samples) and 2.6 eV for powdered samples)) [63, 64] due to limited visible light absorption and the low utilization of visible-light-excited high-level energy electrons [65]. Hence, the research has been aimed to improve its photocatalytic properties by altering its surface properties (like morphology, size of the particle, and surface area) and metal/nonmetal ions doping into its lattice. $LaFeO_3$ nanoparticles with different morphologies have been synthesized by sol–gel method [66], sonochemical method [67], electrospinning method [68], polymeric precursor route [69], and hydrothermal method [70, 71] to improve its catalytic, magnetic, and photocatalytic properties. Shudan Li and Xianlei Wang have prepared one-dimensional $LaFeO_3$ fibers with different morphologies by electrospinning method. They have reported the concentration effect of acetic acid and ferric nitrate solutions on the morphology of $LaFeO_3$. The effects of morphology on photocatalytic activity have also been investigated [69]. The introduction of metal ion substitution in place of La/Fe in $LaFeO_3$ on its photocatalytic activity has also been explained [72–76]. Parrino et al. synthesized Cu-substituted $LaFeO_3$ perovskites ($LaFe_{1-x}Cu_xO_{3-\delta}$, where x = 0.05, 0.10, 0.20, and 0.40) by citrate auto-combustion method and discussed their photocatalytic activity by employing 2-propanol oxidation in the gas–solid regime as a probe reaction. They concluded that the

photocatalytic activity of the Cu(II)-substituted $LaFeO_3$ is improved by increasing the Cu amount up to 10 mol% and slightly decreased for higher copper contents. The higher activity of Cu(II)-substituted $LaFeO_3$ compared to that of pristine $LaFeO_3$ has been related with the presence of oxygen vacancies and with the reduced electron–hole recombination [77]. It was reported that the catalytic activities of the manganese-substituted $LaFeO_3$ were much higher than pure $LaFeO_3$ because of its higher oxygen vacancies, the variable valency of Mn ions, and the strong absorption in visible light [75]. Jauher et al. reported the synthesis of $LaMn_xFe_{1-x}O_3$ (x = 0.0–0.5) and examined their H_2O_2-assisted catalytic cationic and anionic dye degradation in the presence and absence of visible light irradiation. They observed that all the Mn-substituted ferrite compositions catalyzed the degradation of dyes both in the absence and presence of visible light irradiation and stated that the catalytic activity is not influenced significantly with increasing manganese content. $LaMn_{0.2}Fe_{0.8}O_3$ exhibited excellent photocatalytic activity for the degradation of both cationic and anionic dyes [78]. Based on these results, Dhiman et al. studied photocatalytic properties of the transition metals doped with $LaMn_{0.2}Fe_{0.8}O_3$ ($LaMn_{0.2}M_{0.2}Fe_{0.6}O_3$ (M = Cr^{3+}, Co^{2+}, Ni^{2+}, Cu^{2+}, and Zn^{2+})). All $LaMn_{0.2}M_{0.2}Fe_{0.6}O_3$ compositions (except M = Cr) have shown higher photocatalytic dye degradation which is attributed to the generation of vacancy defects and smaller band gap energy values [79].

Xicai Hao and Yongcai Zhang have synthesized porous nano-$LaFeO_3$ through a gel combustion method at the calcination temperatures of 200–400 °C and studied the photocatalytic reduction of aqueous Cr(VI) under visible light irradiation. The $LaFeO_3$ prepared at lower temperature exhibited enhanced photocatalytic activity in the reduction of Cr(VI) in aqueous solution under visible light irradiation [80]. Giuseppina et al. prepared $LaFeO_3$ nanoparticles via solution combustion method and investigated their photocatalytic efficiency for hydrogen production from glucose aqueous solution under UV and visible light emitted by light-emitting diodes (LEDs) [81]. Stable $LaFeO_3$ nanoparticles with a size of 15 nm and the band gap of 1.86 eV have been prepared by a sol–gel method using reduced graphene oxide (rGO) as a template by Ren et al. [82]. They have demonstrated that $LaFeO_3$–rGO can function as an efficient catalyst for degradation of methylene blue (MB) or rhodamine B (RhB) under visible light irradiation. From the controlled photocatalytic experiments, it was concluded that electron transfer from the dye molecule to hole dominated the oxidation process.

To overcome the low utilization of visible-light-excited high-level energy electrons (HLEEs) and limited visible light absorption of $LaFeO_3$, Muhammad et al. prepared ZnO-coupled Bi-doped porous $LaFeO_3$ and evaluated its visible light photocatalytic performance for 2,4-dichlorophenol (2,4-DCP) degradation and CO_2 conversion. The improved visible light activity is endorsed to the improved utilization of visible-light-excited HLEEs by protracting visible light absorption via the Bi-introduced surface states and coupling ZnO to introduce a suitable high-level-energy platform for accepting electrons. The mechanism of photocatalytic degradation of 2,4-DCP over ZnO/Bi-doped porous $LaFeO_3$ has also been discussed [83]. Yan et al. prepared a p–n heterojunction composed of p-type

$LaFeO_3$ and n-type g–C_3N_4 and studied its photocatalytic activity against Brilliant Blue (BB) degradation under the visible light irradiation. The improved photoactivity of g–C_3N_4 and $LaFeO_3$ is attributed to efficient separation of electron–hole pairs, a higher concentration of superoxide and hydroxyl radicals. Electron spin resonance (ESR) analysis and the active species trapping experimental results confirmed the Z-scheme photogenerated electron transfer mechanism integrated with the dye-sensitization effect of the photocatalytic reaction process [43]. Ibrahim et al. prepared n-type $LaFeO_3$ and evaluated its photoelectrochemical water splitting under simulated AM 1.5G solar illumination in view of factors influencing photocatalytic performance including the calcination temperature, the species, concentration, and the pH of the electrolyte that are evaluated [84].

A perovskite, lanthanum cobaltite ($LaCoO_3$), is considered as a promising catalytic material because of its appealing physicochemical properties such as electrical, ionic conductivities, and excellent electrochemical properties [85, 86]. But less visible light-harvesting, higher electron–hole recombination rates and a short lifetime of photogenerated charge carriers hindered its pragmatic applications. Feng et al. adopted sol–gel and deposition–precipitation method to get a PdO/$LaCoO_3$ heterojunction photocatalyst to enhance the H_2 production from formaldehyde aqueous solution without any additives at low temperature. The heterojunction structure can significantly improve the charge generation, enhance the visible light absorption, and efficiently confine the recombination of photogenerated electron–hole pairs to exhibit higher photocatalytic activity. The obtained results are demonstrated that PdO doping on the $LaCoO_3$ surface can effectively adjust band gap and Fermi energy levels to apply in hydrogen production from formaldehyde solution under visible light. It is found that the hydrogen production rate of 2 wt% PdO/$LaCoO_3$ is multiple of ten higher than pristine $LaCoO_3$ [87].

Minghui Wu et al. tried to prepare $LaCoO_3$ with propitious performance through creating oxygen vacancies in it. $LaCoO_3$ is prepared using natural sugarcane bagasse with tunable oxygen vacancy and enlightened the interaction between metal ions and sugarcane bagasse [88]. It has been stated that natural biomass like sugarcane bagasse and extract of Pichia pastoris GS115 may not only replace the usual chemical reagents because of the benefits of being green, environmental, and low cost but also provide ample functional groups to interact with the metal ions leading to varying in the surface properties, and even form a unique structure of the synthesized photocatalysts, which could tune the amount of oxygen vacancy and bring the lattice defects [89]. The characterization of bagasse is carried out to explicate its interaction with metal ions and role in the synthesis process. Moreover, the correlation between the amount of oxygen vacancy on the perovskite induced by biomass and the performance of photocatalytic hydrogen production is examined and reported that as-synthesized sugarcane bagasse-mediated $LaCoO_3$ perovskite had worthy photocatalytic performance in hydrogen production from formaldehyde solution under visible light irradiation than that prepared by conventional citric acid method [88]. Liqing et al. reported novel microbial synthesis of high efficient Cu-doped $LaCoO_3$ photocatalyst from Pichia pastoris GS115 for hydrogen production from formaldehyde solution under visible light irradiation. Copper doping

favors the formation of impurity level and appropriate oxygen vacancy. The biomass intervention in synthesis assists the adjustment of the crystal structure and surface structure of catalyst, which makes the diffraction angle and unit cell change and simultaneously regulates surface oxygen defects. Besides, the abundant organic functional groups from biomass residue on the surface act as a photosensitizer, so that the higher photocatalytic performance is obtained for the catalyst prepared by microbial synthesis than the catalyst prepared by traditional chemical methods [90]. Jayapandi et al. prepared pristine and silver (Ag)-modified $LaCoO_3$ via a hydrothermal process. Silver is considered as better metal dopant because Ag can induce transport of charge carriers and acts as an effective carbon removal, better photo absorber and provide active species for oxygen activation. Ag-modified $LaCoO_3$ degraded methylene blue (MB) in higher rate (99% in 10 min) compared to pure $LaCoO_3$ (75% in 10 min) [91].

The photodegradation of methyl orange within 90 min of visible light irradiation is observed using pure $LaMnO_3$ nanoparticles [92]. It is well known that the porous perovskite oxides with the improved specific surface area are vital to increasing the photocatalytic activity [93, 94]. Rajesh Kumar et al. examined the significance of different morphologies of $LaMnO_3$ particles for the degradation of RB dye under visible light irradiation. As-prepared porous $LaMnO_3$ nanoparticles degraded 95% of RB dye in 60 min of irradiation time. These results imply that the porous morphology and specific surface area plays a key role in the photocatalytic performance [95]. Peisong et al. studied the photodegradation of methyl orange dye under the visible light irradiation using $YbFeO_3$ [96] and $EuFeO_3$ [97].

The structural features of $BaZrO_3$ like ideal cubic crystalline phase with a bond angle of 180° of the ZrO_6 octahedral sites and largely dispersed conduction band have provoked to study its photocatalytic activity. Yupeng et al. studied for the first time the photocatalytic water splitting of $BaZrO_3$ under the UV light irradiation [98]. Later, the same group has tried to modify the electronic structure of $BaZrO_3$ to enhance the evolution rate of H_2 by doping Sn^{4+} in Zr^{4+} site. They observed that $BaZr_{0.7}Sn_{0.3}O_3$ exhibits the highest H_2 evolution rate [99]. They have also investigated the impact of Sr^{2+} substitution on photocatalytic water splitting activity of $BaSnO_3$ [100]. Borse et al. switched the UV active $BaSnO_3$ photocatalyst into a visible-light-active photocatalyst for O_2 production through the electronic structure modification by doping Pb^{2+} for Sn^{2+} [101]. Subsequently, attempts have been made to improve the photocatalytic activity of $BaZrO_3$ not only by metal ion doping [102, 103] but also preparing $BaZrO_3$ solid solutions [ex: $BaZrO_3$–$BaTaO_2N$ Solid-Solution Photocatalyst] [104] or heterojunction formation with other metal oxides [Ex: $BaZrO_3/Cu_2O/Bi_2O_3$] [105].

Titanium-based perovskite materials with the composition of $ATiO_3$ (A = Sr, Ca, and Ba) have been studied for photocatalytic applications for a long time even though having wide band gap energies due to their excellent resistance to photo-corrosion and high thermal stability [106]. Among the large number titanate perovskites, strontium titanate oxide ($SrTiO_3$) with an indirect band gap of 3.25 eV has been one of the most studied photocatalysts, exhibiting an unusual photocatalytic activity in various photocatalytic applications [107, 108]. Many researchers

have attempted to tune the electronic structure of titanium-based perovskite oxides to obtain the improved photocatalytic activity. Here, the recent developments in enhancing the photocatalytic applications of $ATiO_3$ (A = Sr, Ca, and Ba) have been presented.

A series of Au/$SrTiO_3$ nanocomposites with different Au contents have been synthesized by Xian et al., using a photocatalytic reduction method. The photocatalytic activity of the obtained composites was investigated for the photocatalytic degradation of acid orange 7 and methyl orange dyes under simulated sunlight and visible light irradiation, and a higher photoactivity observed for Au/$SrTiO_3$ nanocomposite than that of pure $SrTiO_3$ [109]. Liu et al. successfully synthesized WO_3, nanosheets with different SrTiO3 (La, Cr) contents. The photocatalytic activity of the as-prepared samples was measured in the decomposition of methylene blue under visible light irradiation [110]. Kissa et al. synthesized $SrTi_{1-x}Rh_xO_3$ photocatalyst considering different Ti/Rh ratios using a one-step hydrothermal synthesis and studied for the decomposition of methyl orange under visible light irradiation. 5% Rh-doped $SrTiO_3$ is shown to completely oxidize methyl orange within 30 min under visible light illumination [111]. Pure TiO_2, $SrTiO_3$, and $SrTiO_3$/TiO_2 nanocomposite were prepared by Devi et al. through a sol–gel method. The photoactivity of the as-prepared samples was evaluated by the degradation of 4-Nitrophenol (4-NP) under UV light irradiation, which revealed that the composite had improved photoactivity as compared to pure TiO_2 and $SrTiO_3$ [112]. Swapna et al. examined photocatalytic degradation of methylene blue under UV light with $SrTiO_3$ catalysts. The $SrTiO_3$ catalysts were prepared by a novel polymerizable sol–gel (PSG) approach for the first time [113]. $SrTiO_3$ powders were prepared by applying a polymeric precursor method by Silva et al. for the photocatalytic decomposition of methylene blue (MB), rhodamine B (RhB), and methyl orange (MO) dyes under UV illumination [108].

Goto et al. studied the photocatalytic decomposition of water over Al-doped $SrTiO_3$ ($SrTiO_3$:Al) catalyst under solar light irradiation [114]. The heterojunction semiconducting Au–Al/$SrTiO_3$ oxide was prepared by Saadetnejad et al. for hydrogen production by photocatalytic water splitting under visible light in the presence of methanol, ethanol, and isopropyl alcohol as sacrificial agents. They synthesized the Al/$SrTiO_3$ via solid-state reaction, while Au loading was done with the homogenous deposition–precipitation method. The results showed that the 0.25% Au–1.0% Al/$SrTiO_3$ composite oxide exhibited higher photocatalytic hydrogen evolution of 347 mmol/h with isopropyl alcohol as sacrificial agent [115]. Han et al. prepared Mg-modified $SrTiO_x$ photocatalysts by solid-state method. The samples were shown excellent performance for the photocatalytic water splitting under solar light illumination and the maximum H_2 evolution activity was obtained with the $Sr_{1.25}Mg_{0.3}TiO_x$ material [116].

Pure $SrTiO_3$ is not considered as a good photocatalyst because it is only active under UV irradiation, and therefore cationic/anionic dopants are often doped into $SrTiO_3$ to make it visible light-responsive. Kou et al. used the transition metal ions such as Co, Fe, and Ni as dopants to improve the photocatalytic CO_2 reduction to CH_4. Among the dopants, Co ions doped $SrTiO_3$ displays the most outstanding

photocatalytic performance for CO_2 photoreduction. Photo-deposition of Pt metal ions on co-doped $SrTiO_3$ surface further improves the CO_2 reduction to CH_4, and the yield of CH_4 under visible light irradiation is 63.6 ppm/h [117]. Luo and co-workers reported three kinds of $SrTiO_3$-containing ($SrTiO_3$, surface-Ti-rich $SrTiO_3$, and $Sr(OH)_2$-decorated $SrTiO_3$) photocatalysts for CO_2 reduction with H_2O vapor under visible light irradiation. They found that the molecular oxygen and CO were only the photoreduction products and the surface-Ti-rich $SrTiO_3$ exhibits the highest photocatalytic activity for CO_2 reduction [118]. By taking advantage of the loading/deposition of other metal or metal oxides on $SrTiO_3$ semiconductors, Li et al. prepared Rh and Au co-loaded $SrTiO_3$ through a photo-deposition process and studied the as-prepared catalysts for synthesis of syngas (CO and H_2) from photocatalytic reduction of CO_2 with water vapor under visible light irradiation [119]. Shoji et al. prepared the strontium titanate ($SrTiO_3$: STO) nanorod thin films loaded with amorphous copper oxide (CuO_x) nanoclusters. They found that compared to bare STO nanorods, the loading of the CuO_x-cocatalysts onto STO nanorods improved the photocatalytic carbon dioxide (CO_2) reduction using H_2O as an electron donor into carbon monoxide (CO) [120].

It is realized that the photocatalysts with a three-dimensional (3D) porous microsphere structure exhibited a high photocatalytic performance because they possess a high specific surface area and plenty of active sites for the target reaction, absorb more light through the reflection of pore walls, and are easy to be recycled by facile mechanical filtration [121]. Yang et al. prepared porous $SrTiO_3$ microsphere through a sol–gel method and observed its high photocatalytic performance for the Cr(VI) reduction under UV light irradiation [122]. Later, they tried to extend the photo-response of three-dimensional (3D) porous $SrTiO_3$ microspheres to the visible light region, thus enhancing their visible light photocatalytic activity [123]. They prepared three-dimensional porous La-doped $SrTiO_3$ (LST) microspheres via a modified sol–gel method. The agarose gel/$SrCO_3$ microsphere and La_2O_3 were used as the template and the La resource, respectively. The morphology of as-prepared LST-0.5 (agarose gel/$SrCO_3$/0.5 wt% of La_2O_3) sample is shown in Fig. 6. It is observed that these microspheres exhibit a higher photocatalytic activity than the undoped $SrTiO_3$ sample for the reduction of Cr(VI) under visible light irradiation. They have concluded that the observed redshift of absorption edge of $SrTiO_3$ inhibits the recombination of photogenerated electrons and holes, leading to the higher photocatalytic activity under visible light. Among all the as-prepared LST samples, LST-0.5 reduced 84% Cr(VI) within 100 min, exhibiting the highest photocatalytic activity. It is evident from Fig. 7 that the LST-0.5 sample has an excellent reusability, which may lay a good foundation for their practical application. They have also suggested photocatalytic mechanism for the reduction of Cr (VI) by porous LST microspheres under visible light as shown in Fig. 8.

Oxide mineral calcium titanate ($CaTiO_3$) was discovered in 1839 in the Ural Mountains and named for Russian mineralogist L. A. Perovski [124]. $CaTiO_3$ has also attracted a great deal of interest in the world of oxide electronics, not only as a functional material in electronic and piezoelectric devices but also as a

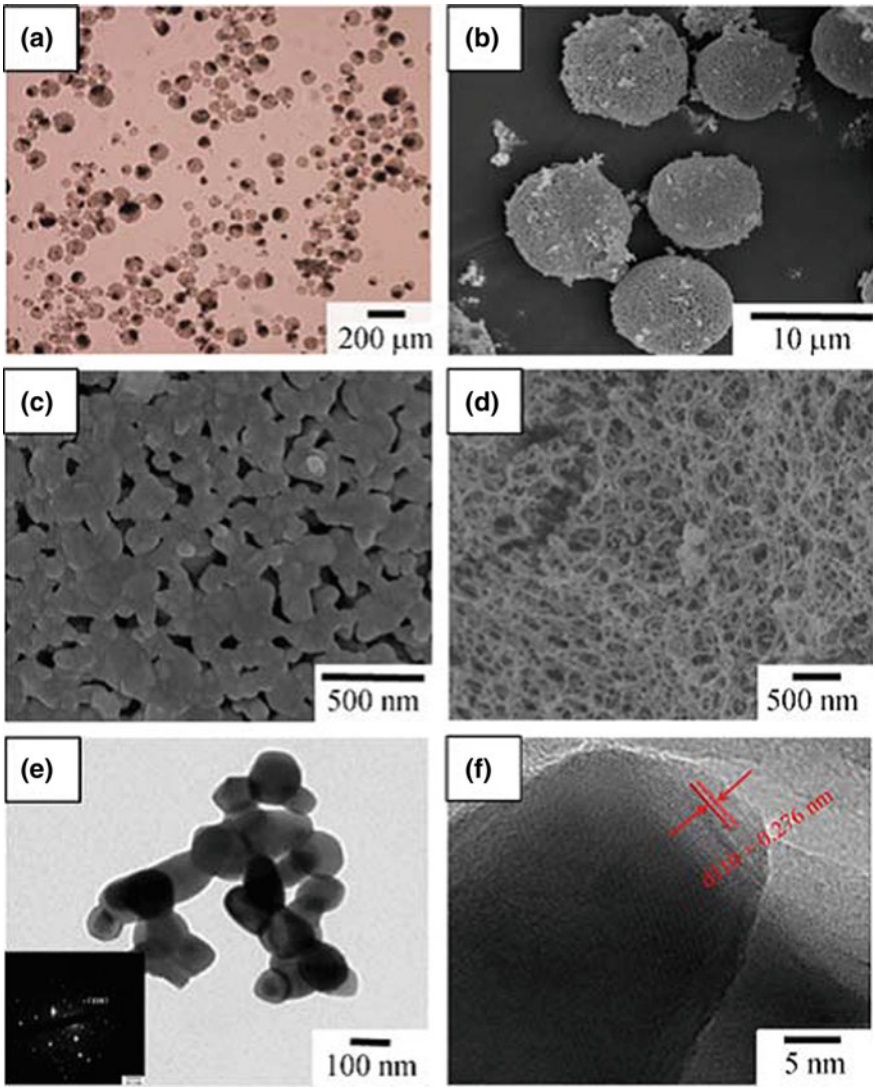

Fig. 6 **a** OM photo of agarose gel/$SrCO_3$/TiO_2/La_2O_3 composite beads; **b** low- and **c**, **d** high-magnification SEM photos of LST (**c**), outside surface; **d**, inner structure; **e** TEM photo with corresponding SAED pattern (inset); **f** HRTEM photo of LST [123] Copyright 2018. Reprinted with permission from Springer Nature

semiconducting material with a band gap of ~3.5 eV. However, due to its wide band gap (3.5 eV), $CaTiO_3$ was rarely used for the photocatalytic applications and its photoactivity is limited to UV excitation only. In the study by Yan et al., surface disorder-engineered $CaTiO_3$ were applied as the semiconducting materials for photocatalytic degradation of rhodamine B (RhB) under irradiation of simulated sunlight

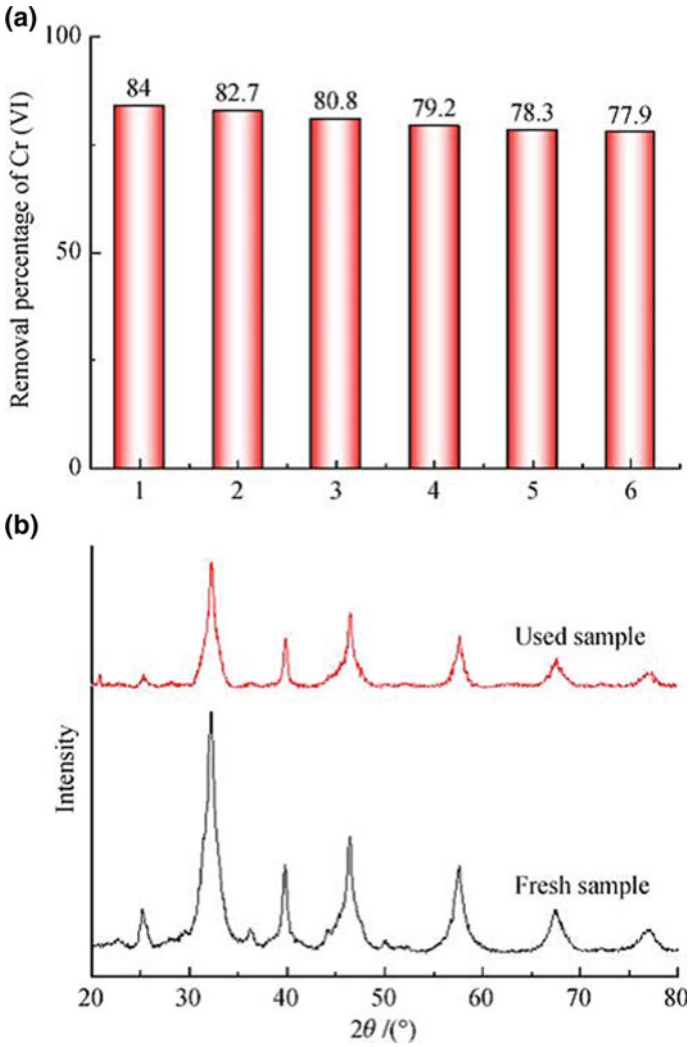

Fig. 7 **a** Recycling test of LST-0.5 for photocatalytic reduction of Cr(VI) under visible light and **b** XRD patterns of LST before and after six recycling tests [123] Copyright 2018. Reprinted with permission from Springer Nature

and UV light [125]. Graphitic carbon nitride (g–C_3N_4)–$CaTiO_3$ heterojunction photocatalysts were synthesized by Kumar et al. for the photocatalytic decomposition of rhodamine B (RhB) under UV, visible, and natural sunlight irradiation. The $CaTiO_3$ (CT) nanoflakes were homogeneously deposited onto the surface of g–C_3N_4 nanosheets by using a facile mixing method [126]. Yan et al. reported a facile hydrothermal approach to synthesize $CaTiO_3$ nanocuboids of controlled sizes that were used for degradation of rhodamine B under simulated sunlight irradiation.

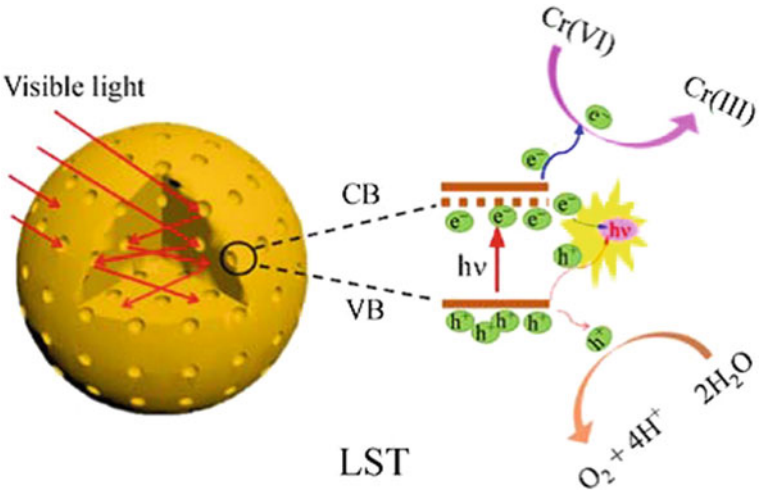

Fig. 8 Proposed photocatalytic mechanism for the reduction of Cr(VI) by porous LST microspheres under visible light [123] Copyright 2018. Reprinted with permission from Springer Nature

The photoactivity results demonstrated that $CaTiO_3$ nanocuboids exhibit superior photocatalytic activity when compared with $CaTiO_3$ nanoparticles [127]. Han et al. prepared an orthorhombic $CaTiO_3$ by solid-state, sol–gel, and hydrothermal methods and studied their photocatalytic performance for the degradation of methylene blue (MB) in an aqueous solution under the irradiation of visible light [128]. The photocatalytic activity of Ag–La co-doped $CaTiO_3$ powder for hydrogen evolution under UV and visible light was studied by Zhang et al. The photocatalyst, Ag–La co-doped $CaTiO_3$, showed higher H_2 production activity than that of pure $CaTiO_3$ powder [129]. Im et al. synthesized $CaTiO_3$@basalt fiber (BF) materials through a facile dipping method. This catalyst achieved high photocatalytic activity in CO_2 reduction (CH_4 = 17.8 μmol/g, CO = 73.1 μmol/g) [130]. Similarly, Yoshida et al. studied the composite catalysts of $CaTiO_3$@basalt fiber (BF) materials, consisting of $CaTiO_3$ with various Ca/Ti ratios, for CO_2 photochemical reduction. $CaTiO_3$ (1.5:1)@BF, had superior CO_2 adsorption and also the best CO_2 reduction performance (CH_4 = 17.8 μmol/g and CO = 73.1 μmol/g) [131].

The photocatalytic applications of Barium titanate, $BaTiO_3$, are limited due to its wide band gap energy in the range of 3.7–3.8 eV. Selvarajan et al. synthesized the novel $BaTiO_3$–SnO_2 nanocomposites by hydrothermal and precipitation deposition method. O-Chloroaniline and methylene blue were used as the model pollutants to evaluate the photocatalytic activity of the as-synthesized samples under UV–Vis light irradiation [132]. Nageri et al. reported the successful synthesis of Mn-doped barium titanate nanotube arrays by hydrothermal method, and the photocatalytic activity of these catalysts was evaluated by studying the degradation of methylene blue (MB) dye under visible light source [133]. Thamima et al. observed the

photocatalytic performance of the $BaTiO_3$ catalysts using various dyes such as Methylene Blue (MB), Malachite Green, and Alizarin Red S under UV light irradiation [134]. Maeda et al. synthesized rhodium-doped $BaTiO_3$ catalysts with five different Rh concentrations (1–5 mol%) by using a polymerized complex (PC) method to sensitize $BaTiO_3$ into visible light. The synthesized catalysts studied for hydrogen production by photocatalytic water splitting under visible light in the presence of methanol as an electron donor [135].

Tantalate-based semiconductor materials, such as alkali tantalates, which have unique crystal and energy band structures, are widely used in photocatalysis. Further, they possess both valence band and conduction band (CB consisting with Ta 5d orbitals at a high potential) potentials suitable for photocatalytic applications. Due to their high photosensitivity, nontoxicity, stability, and commercial availability, these catalysts scores highest among the large band gap semiconductors as a photocatalyst.

$NaTaO_3$ (band gap energy $\sim$4.07 eV) has attracted extensive attention in photocatalytic applications due to its good stability and high photocatalytic activity. Moreover, $NaTaO_3$ is considered as a good host material for developing visible light photocatalysts, especially when doped with rare earth elements like La [136]. Wang et al. reported that W and N co-doped $NaTaO_3$ showed higher photocatalytic activity toward degradation of rhodamine B (RhB) under visible light irradiation than single-element-doped $NaTaO_3$ [137]. Lan et al. reported the photocatalytic activity of the La/Bi co-doped $NaTaO_3$ and pure $NaTaO_3$ materials for the degradation of methylene blue under visible light irradiation. The La and Bi co-doping reduces the particle size, thereby extends the absorption edge toward longer wavelength [138]. A novel sulfur-doped $NaTaO_3$ photocatalyst was successfully synthesized by Li et al. through a simple hydrothermal process, and its photocatalytic activity was evaluated by methyl orange (MO) and phenol degradation processes [139]. The interest in $NaTaO_3$ in water splitting reaction recently increased after the discovery of its photocatalytic properties as water splitting [140]. $NaTaO_3$-based photocatalysts doped with different rare earth metal ions such as Y, La, Ce, and Yb with a constant ratio of rare earth metal ions have been synthesized by Jana and co-workers from the solid-state method and tested their photoactivity toward H_2 production by water/methanol mixture (methanol as an electron donor) under solar light. The higher H_2 production has been obtained with the Y-doped $NaTaO_3$ catalyst. Further, the deposition of Pt nanoparticles as cocatalyst, over these catalysts, improves even further the water splitting activity [141]. The photocatalytic activity of La-doped and pure $NaTaO_3$ in the H_2 evolution under UV light was studied by Lopez-Juarez et al. The higher photocatalytic activity was observed in the 2 mol% La-doped $NaTaO_3$ catalysts [142].

As a functional material, potassium tantalate ($KTaO_3$) has good photocatalytic activity and suitable band gap energy (3.2–3.8 eV). Liu et al. found that the substitution of La for K in $KTaO_3$ ($K_{1-x}La_xO_3$) can significantly improve the activity for methyl orange (MO). They demonstrated that the incorporation of La^{3+} ions in $KTaO_3$ host lattice led to a monotonous lattice contraction and increased the BET surface area [143]. Krukowska et al. investigated the photocatalytic activity of

mono- and bimetallic noble metal nanoparticles (MNPs/BNPs) decorated on the surface of $KTaO_3$ using by hydrothermal reaction of $KTaO_3$ followed by photo-deposition of MNPs/BNPs. The photocatalytic activity was estimated considering three model reactions by measuring the decomposition efficiency of phenol solution, the removal efficiency of gaseous toluene, and amount of evolved H_2 production in the presence of formic acid solution under the presence of Vis or UV–Vis light source [144]. Reduced graphene oxide-$KTaO_3$ (rGO–$KTaO_3$) hybrid composites with various graphene contents have been prepared by Bajorowicz et al. via the hydrothermal method. The photocatalytic activity of the composite was studied by the degradation of phenol under visible light irradiation. The improved photocatalytic activity can be attributed to the photosensitizer role of graphene in the rGO–$KTaO_3$ composites as well as the formation of p–n heterojunctions between p-type rGO and n-type $KTaO_3$ [145].

For the first time, Chen et al. prepared carbon-doped $KTaO_3$ via a simple combination of hydrothermal and calcination processes with glucose as the carbon source and tested the obtained powders in a photocatalytic H_2 generation under simulated sunlight illumination. The excellent photocatalytic hydrogen production should be mostly ascribed to the enhanced separation efficiency of charge carriers. The H_2 production rate was higher for C-doped $KTaO_3$ (592 μmol/h) than pure $KTaO_3$ (228 μmol/h) due to the enhanced separation efficiency of charge carriers [146]. It is generally accepted that methanol is an important industrial feedstock and is derived from the photocatalytic reduction of CO_2 using tantalum-based perovskites. Xiang et al. prepared CuO-patched cubic $NaTaO_3$ (CNTO) photocatalysts with different Cu contents and carried out the photocatalytic reduction of CO_2 to methanol in isopropanol in a self-made batch reactor. The morphologies of pure $NaTaO_3$ nanocubes and nano-CuO-patched $NaTaO_3$ (CNTOs) were observed by SEM and TEM as shown in Figs. 9 and 10. 5 wt% CNTO was found to have the best activity (CH_3OH yield of 1302.22 μmol g/1 h) and product selectivity in converting CO_2 to CH_3OH [147]. Also, authors have proposed the mechanism for photocatalytic reduction of CO2 to methanol on CuO–NaTaO3 photocatalyst (Fig. 11).

Nakanishi et al. studied the photoactivity of a set of Mg-, Ca-, Sr-, Ba-, and La-doped $NaTaO_3$ powders samples prepared by a solid-state method, while Ni, Pd, Rh, Cu, Au, and Ru cocatalysts were loaded in situ on doped photocatalysts by photo-deposition method, in photocatalytic CO_2 reduction to form CO using water as an electron donor. The best photocatalytic CO evolution obtained with Ag-loaded doped-$NaTaO_3$ photocatalysts [148].

Shao et al. synthesized highly efficient potassium tantalate ($KTaO_3$) materials, from a single-step hydrothermal method and investigated their activities in the reduction of carbon dioxide to methanol in isopropanol under UV light irradiation. Further, they found that the photoactivity of $KTaO_3$ increased with the loading of different NiOx contents and 2 wt% of NiO/$KTaO_3$ sample exhibited highest methanol formation [149]. Li et al. synthesized $KTaO_3$ (KTO)-based samples by

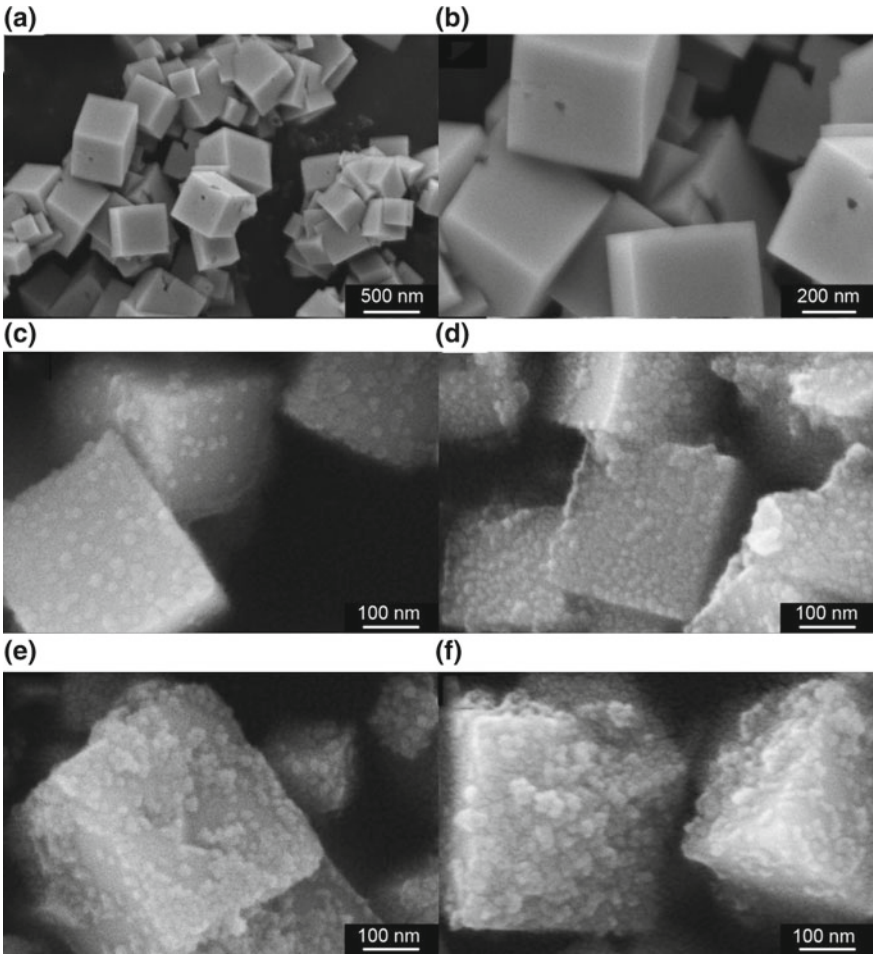

Fig. 9 SEM images: **a**, **b** pure $NaTaO_3$, **c** 2 wt% CNTO, **d** 5 wt% CNTO, **e** 7 wt% CNTO, **f** 10 wt% CNTO [147] Copyright 2018. Reprinted with permission from Elsevier

solid-state reaction (SSR-KTO) and solvothermal methods in hexane–water mixture (Hex-KTO) and ethanol (Eth-KTO) to reduce CO_2 with water under UV light irradiation. KTO prepared in hexane–water mixture sample with a nanoflake-like structure was found to have the best activity (20 times (H_2) and 7 times (CO)) and product selectivity in converting CO_2 to H_2/CO in comparison to other samples [150]. Fresno et al. compared the photocatalytic activity of $NaNbO_3$ and $NaTaO_3$ catalysts in the reduction of CO_2 under UV irradiation and found that the $NaTaO_3$ exhibits better photocatalytic properties regarding $CO/H_2/CH_3OH/CH_4$ (CO was the major product) product selectivity [151].

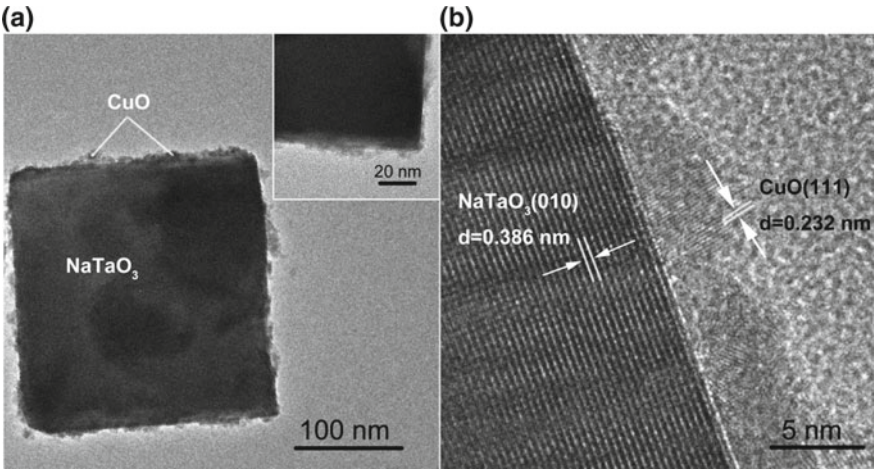

Fig. 10 **a** TEM image and **b** HRTEM image of 5 wt% CNTO [147] Copyright 2018. Reprinted with permission from Elsevier

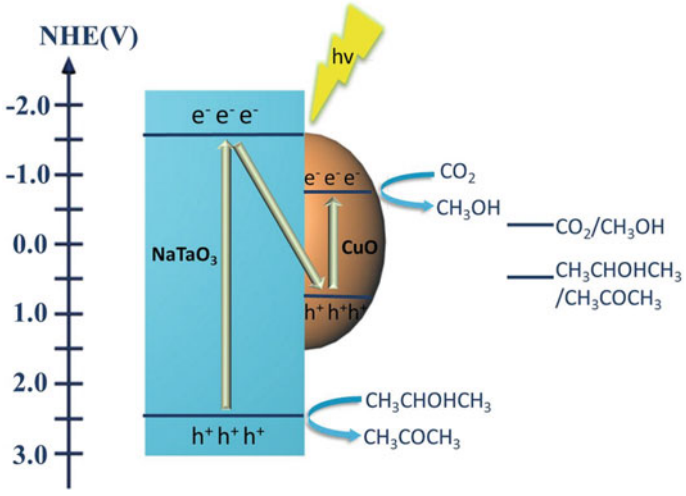

Fig. 11 The proposed mechanism for photocatalytic reduction of CO_2 to methanol on CuO–$NaTaO_3$ photocatalyst [147] Copyright 2018. Reprinted with permission from Elsevier

The niobium-based perovskite materials have been regarded as a potential candidates for a variety of photocatalytic applications compared to that of TiO_2 because the conduction band in niobates perovskite materials consists of Nb 4d which are situated at more negative potential (compared to TiO_2), thereby ensuring the separation and transfer of photoinduced charge carriers very precisely in their

photocatalytic applications. $NaNbO_3$, possibly the most studied of the alkali niobates, is a well-known transparent semiconductor (with a band gap of 3.7 eV) with extremely technological importance. The photocatalytic activity of alkali niobates under UV radiation strongly depends on the nature of the "A" cation. If the A-site in alkali niobates is replaced by Ag ion, it extends the light absorption to visible region and improves the photocatalytic efficiency of alkali niobates. $AgNbO_3$ has a band gap of 2.7 eV, and thus it absorbs visible light. Wu et al. synthesized microcrystalline $AgNbO_3$ photocatalysts as a visible light photocatalyst for the photocatalytic decomposition of cationic dyes such as rhodamine B and methyl blue [152].

Sun et al. synthesized BiOI/$NaNbO_3$ p–n junction photocatalyst at low temperature by using a facile chemical bath method. The photocatalytic activity of the BiOI/$NaNbO_3$ composites was investigated for the degradation of MB under visible light irradiation [153]. $NaNbO_3$ with cubic crystal structure photocatalyst was synthesized by Chen et al. via a convenient solvothermal method and then Ru nanoparticles were added to it by photo-deposition technique. The photocatalytic activity of Ru/$NaNbO_3$ composite was exhibited outstanding performance for the degradation of RhB under visible light irradiation than that of naked and Ru-doped $NaNbO_3$ [154]. For the photodegradation of methylene blue (MB), Wang et al. fabricated cubic $NaNbO_3$ (c-$NaNbO_3$) photocatalyst at 350 °C by a surface ligand-assisted localized crystallization (SLALC) method. They found that the as-synthesized c-$NaNbO_3$ nanoparticles could adsorb 95% of methylene blue in 3 min and photodegrades 99.3% of methylene blue (MB) in 180 min [155]. Liu et al. investigated and compared wire- and cube-like $NaNbO_3$ perovskite catalysts with Pt loading for photocatalytic H_2 production and organic-pollutant degradation. It was found that after the incorporation of Pt NPs, the Pt/$NaNbO_3$ systems exhibited noticeably higher performance due to the better light absorption and the improved separation capability of photogenerated electron–hole pairs [156]. Liu et al. synthesized single-crystalline $NaNbO_3$ with wire- and cube-like morphology by a facile and eco-friendly route including a hydrothermal as well as in-site self-assembled process via optimizing thermal treatment temperature. Photocatalytic activity of as-synthesized samples was measured in the photocatalytic water splitting of H_2 under solar light irradiation. They have found that the photocatalytic activity of $NaNbO_3$ with wire morphology showed the highest H_2 evolution rate (330.3 μmol/g) among all the studied samples. The enhanced photoactivity of $NaNbO_3$ was mainly due to the good crystallinity, fewer defects, and perfect 1D nanowire morphology [157]. The research group led by Li et al. used a polymerized complex method to prepare three $NaNbO_3$ samples that structurally differed from each other: cubic and orthorhombic and mixed cubic–orthorhombic. The sample that consisted of mixed-phase $NaNbO_3$ showed the highest activity in CO_2 reduction to CH_4. The authors explained the enhanced catalytic activity was attributed to the cubic–orthorhombic surface junctions which improved the charge separation [158]. The design of composite photocatalysts, in particular with

graphitic carbon (g–C_3N_4), has recently become most popular in research into the photocatalytic properties of niobate-based semiconductors. Shi et al. used this route to modify the photocatalytic properties of $NaNbO_3$/$KNbO_3$ semiconductors. They prepared g–C_3N_4/$NaNbO_3$ nanowire heterojunction photocatalyst via introducing polymeric g–C_3N_4 on $NaNbO_3$ nanowires (prepared by hydrothermal method) tested their photoactivity in reduction of CO_2 to CH_4 under visible light irradiation. They found that the g–C_3N_4/$NaNbO_3$ heterojunction exhibits the best photocatalytic performance than that of individual g–C_3N_4 and $NaNbO_3$ [159]. Similarly, Shi and his co-workers reported the photocatalytic reduction of CO_2 to CH_4 under visible light illumination, using g–C_3N_4/$KNbO_3$ composites as catalysts. The g–C_3N_4/$KNbO_3$ composite had more photocatalytic activity for CO_2 reduction to CH_4 as compared to pure g–C_3N_4 and $KNbO_3$ under similar reaction conditions [160].

Potassium niobate, $KNbO_3$, has also been reported as a UV light sensitive photocatalyst because of its wide band gap energy (3.14 eV). Raja et al. prepared Bi-doped $KNbO_3$ powders by the solid-state reaction by varying the ratio of K/Bi in starting materials and tested their photocatalytic activity in the degradation of methyl orange (MO) aqueous solution under UV light. They found that the photocatalytic degradation of Bi-doped $KNbO_3$ was 2.25-fold higher than that of pure $KNbO_3$ and this can due to increased BET surface area, crystallite size, and band gap alteration of the $K_{1-x}Bi_xNbO_3$ [161].

Zhang et al. reported the photocatalytic H_2 evolution from aqueous methanol with a micro-cubic structured potassium niobate ($KNbO_3$) semiconductor system under the illumination of visible light [162]. Nitrogen doping is an effective method for modifying light absorption behavior of wide band gap semiconductors. In view of this, N-doped $NaNbO_3$ nanocube structured powders were obtained by Wang et al. by applying a simple hydrothermal method. The photocatalytic activity of the N-doped $KNbO_3$ and pure $KNbO_3$ has been evaluated by photocatalytic water splitting as well as degradation of four organic contaminants (rhodamine B, orange G, bisphenol A, and pentachlorophenol) under visible light irradiation [163]. Hong et al. established a visible-light-driven photocatalytic system comprised of potassium niobate microspheres and reduced graphene oxide ($KNbO_3$/RGO) for hydrogen evolution. The hybrid nanocomposite ($KNbO_3$/RGO) exhibited the highest H_2 evolution rate compared to pure potassium niobate microspheres. This enhanced photocatalytic efficiency was attributed mainly to the proficient separation of photogenerated carriers at the heterojunction of two dissimilar semiconductors [164]. We have provided a Table 1 containing the photocatalytic activity results of recently published literatures (Years: 2015–2018) on ABO_3-type photocatalysts.

Table 1 Photocatalytic activity results of recently published (Years: 2015–2018) ABO_3 type photocatalysts

Sample	Preparative conditions	Photocatalytic reaction	Light source	References
Hetero-structured $LaFeO_3$/g–C_3N_4	Quasi-polymeric calcination method with the aid of electrostatic self-assembly interaction	Degradation of brilliant blue (BB)	300 W Xenon lamp with an UV cutoff filter ($\lambda > 420$ nm)	[43]
Cu-substituted $LaFeO_3$	Citrate auto-combustion	Degradation of 2-propanol	1500 W high-pressure Xenon lamp	[78]
Mn-substituted $LaFeO_3$	Sol–gel auto-combustion method	H_2O_2-assisted degradation of cationic and anionic dyes	Visible light	[79]
Transition metals (M = Cr^{3+}, Co^{2+}, Ni^{2+}, Cu^{2+} and Zn^{2+}) doped $LaMn_{0.2}Fe_{0.8}O_3$	Sol–gel auto-combustion route	H_2O_2-assisted degradation of cationic and anionic dyes	Visible light	[80]
$LaFeO_3$	Gel combustion method	Reduction of Cr(VI) in aqueous solution	Visible light (wavelength longer than 420 nm)	[81]
$LaFeO_3$	Solution combustion synthesis	Photocatalytic conversion of glucose to H_2	UV–LEDs (nominal power: 10 W) with wavelength emission in the range 375–380 nm	[82]
$LaFeO_3$–reduced graphene oxide nanoparticles (rGO NPs)	Reduced graphene oxide (rGO) as a template and high-temperature sol–gel method	Degradation of methylene blue (MB) or rhodamine B (RhB)	300 W xenon arc lamp with a UV-cutoff filter ($\lambda > 400$ nm)	[83]
ZnO/Bi-doped porous $LaFeO_3$ nanocomposites	Wet chemical method	2,4-dichlorophenol (2,4-DCP) degradation and CO_2 conversion	150 W GYZ220 high-pressure Xenon lamp $\lambda = 420$ nm	[84]
PdO/$LaCoO_3$ heterojunction	Sol–gel and deposition precipitation method	Hydrogen production from formaldehyde aqueous solution	125 W Xe lamp	[88]
$LaCoO_3$	Sugarcane bagasse hydrolysis by metal ions mediated process	Hydrogen production from formaldehyde solution	125 W Xe lamp	[90]
Cu-doped $LaCoO_3$	Microbial synthesis using the extract of Pichiapastoris GS115	Hydrogen production from formaldehyde solution	125 W Xe lamp	[91]

(continued)

Table 1 (continued)

Sample	Preparative conditions	Photocatalytic reaction	Light source	References
Ag-modified $LaCoO_3$	Hydrothermal method	Degradation of methylene blue (MB)	Sunlight	[92]
Porous $LaMnO_3$ sub-micron particles	Hydrothermal process	Degradation of rose bengal dye	150 W mercury lamp ($\lambda > 400$ nm)	[96]
$YbFeO_3$	Sol–gel process	Decomposition of methyl orange (MO)	150 W Xe lamp	[97]
$EuFeO_3$	One-step microwave route	Decomposition of methyl orange (MO)	Metal halogen lamp (150 W) equipped with a JB400 filter	[98]
$BaZrO_3$ modified with Cu_2O/Bi_2O_3 quantum dots	Hydrothermal process followed by chemical reduction	Phenol photodegradation process in the liquid phase under UV–Vis and toluene degradation in the gas phase under visible irradiation	High-pressure mercury lamp (Heraeus, 150 W) for liquid-phase reaction and An array of 5 Vis LEDs ($\lambda_{max} = 415$ nm) for gas-phase reaction	[105]
$SrZrO_3$ modified with Cu_2O/Bi_2O_3 quantum dots	Hydrothermal process followed by chemical reduction	Phenol photodegradation process in the liquid phase under UV–Vis and toluene degradation in the gas phase under Vis irradiation	High-pressure mercury lamp (Heraeus, 150 W) for liquid-phase reaction and An array of 5 Vis LEDs ($\lambda_{max} = 415$ nm) for gas-phase reaction	[105]
Au/$SrTiO_3$ nanocomposites with different Au contents	Photocatalytic reduction method	Degradation of acid orange 7 and methyl orange (MO)	Sunlight (200 W xenon lamp) and visible light ($\lambda = 420$ nm)	[110]
$SrTiO_3$ (La,Cr)-decorated WO_3 nanosheets	Sol–gel hydrothermal method	Degradation of methylene blue (MB)	Visible light (300 W Xe lamp; $\lambda = 420$ nm)	[111]
$SrTi_{1-x}Rh_xO_3$	Hydrothermal synthesis	Degradation of methyl orange (MO)	Visible light (300 W Xe lamp (Oriel); $\lambda > 420$ nm)	[112]
$TiO_2/SrTiO_3$ nanocomposite	Sol–gel method	Degradation of 4-Nitrophenol (4-NP)	UV light (medium pressure Hg vapor lamp of 125 W)	[113]
$SrTiO_3$	Polymerizable sol–gel (PSG) approach	Degradation of methylene blue (MB)	UV light (medium pressure Hg vapor lamp of 125 W)	[109]

(continued)

Table 1 (continued)

Sample	Preparative conditions	Photocatalytic reaction	Light source	References
$SrTiO_3$	Polymeric precursor method	Degradation of methylene blue (MB), rhodamine B (RhB) and methyl orange (MO)	UV illumination (UV lamps (TUV Philips, 15-W; λ = 254 nm)	[114]
Al-doped $SrTiO_3$	Molten-salt synthesis	Decomposition of water to H_2 production	Sunlight	[115]
Au/Al–$SrTiO_3$ heterojunction	Solid-state reaction	Hydrogen production using sacrificial agents	Visible light (150 W xenon lamp)	[116]
Mg-modified $SrTiO_x$	Solid-state method	Hydrogen production	Solar light (AM 1.5 G solar simulator; λ = 300–900 nm)	[117]
Co, Fe, and Ni-doped $SrTiO_3$	Combined hydrothermal and solid-state reaction	CO_2 reduction to CH_4	Visible light (300 W Xe lamp; λ > 420 nm)	[118]
Different $SrTiO_3$	Hydrothermal method	CO_2 reduction with H_2O vapor	Visible light (300 W Xe lamp)	[119]
Rh and Au co-loaded $SrTiO_3$	Photo-deposition process	CO_2 reduction with H_2O vapor to syngas	Visible light (300 W Xe lamp; λ > 400 nm)	[120]
$Cu_xO/SrTiO_3$ nanorod thin films	Hydrothermal method	CO_2 reduction using H_2O to CO	UV light (Hg–Xe lamp, LA-410 UV)	[121]
$CaTiO_3$	Hydrothermal route	Degradation of rhodamine B (RhB)	Simulated sunlight, and Visible light	[126]
g–C_3N_4–$CaTiO_3$	Facile mixing method	Degradation of rhodamine B (RhB)	UV (Luzchem LZC 4 V UV irradiation chamber equipped with 12 UV lamps (λ = 365 nm), visible (two 14 W white light LED bulbs), and natural sunlight irradiation	[127]
$CaTiO_3$ nanocuboids	Hydrothermal approach	Degradation of rhodamine B (RhB)	Simulated sunlight (200 W Xe lamp)	[128]
Orthorhombic $CaTiO_3$	Solid-state, sol–gel, and hydrothermal methods	Degradation of methylene blue (MB)	Visible light (500 W Hg lamp)	[129]
Core–shell structured CaTiO3@basalt fiber	Modified hydrothermal method	CO_2 reduction with H_2O into CH_4 and CO	UV light (6.0 W/cm^2 mercury lamps (365 nm)	[131]

(continued)

Table 1 (continued)

Sample	Preparative conditions	Photocatalytic reaction	Light source	References
$CaTiO_3$@basalt fiber (BF)	Flux method	CO_2 reduction with H_2O into CH_4 and CO	UV to visible light (300 W xenon lamp)	[132]
$BaTiO_3$–SnO_2	Hydrothermal and precipitation deposition method	O-Chloroaniline and methylene blue (MB)	Visible light (300 W Xe arc lamp; $\lambda > 420$ nm)	[133]
Mn-doped $BaTiO_3$ nanotube arrays	Hydrothermal method	Degradation of Methylene blue (MB) dye	Visible light (300 W Tungsten lamp)	[134]
$BaTiO_3$	Microwave-assisted peroxo route	Degradation of methylene blue, malachite green, and alizarin red S	UV light (6 W Hg lamp)	[135]
W and N co-doped $NaTaO_3$	NaOH flux method	Degradation of rhodamine B (RhB)	Visible light (300 W xenon lamp; $\lambda > 400$ nm)	[138]
La/Bi co-doped NaTaO3	Hydrothermal synthesis	Degradation of methylene blue (MB)	Visible light (250 W high-pressure Hg lamp)	[139]
Sulfur-doped $NaTaO_3$	Hydrothermal process	Degradation of methyl orange (MO) and phenol	UV (8-W Hg lamp and Visible light (250 W Hg lamp)	[140]
La-doped $NaTaO_3$	Solid-state method	H_2 evolution	UV light (high-pressure Hg lamp (I_0 = 2 $mW{\cdot}cm^{-2}$)	[143]
La-doped $KTaO_3$	Hydrothermal technology	Degradation of methyl orange (MO)	UV light (300 W lamp)	[144]
Mono- and bimetallic noble metals decorated $KTaO_3$	Hydrothermal reaction	Decomposition of phenol solution, removal of gaseous toluene, and H_2 production in the presence of formic acid solution	Visible (1000 W Xe lamp) or UV–Vis light irradiation (250 W Xe lamp)	[145]
rGO–$KTaO_3$ hybrid composite	Hydrothermal method	Degradation of phenol solution	Visible–light (1000 W Xe lamp)	[146]
Carbon-doped $KTaO_3$	Combination of hydrothermal and calcination process	H_2 generation	Simulated sunlight (300 W Xe lamp)	[147]
CuO-patched cubic $NaTaO_3$	Hydrothermal synthesis followed by phase-transfer protocol and solvothermal method	CO_2 reduction to CH_3OH in isopropanol	250 W high-pressure mercury lamp	[148]

(continued)

Table 1 (continued)

Sample	Preparative conditions	Photocatalytic reaction	Light source	References
Mg-, Ca-, Sr-, Ba-, and La-doped $NaTaO_3$	Solid-state method	CO_2 reduction to CO using water as an electron donor	400 W high-pressure Hg lamp	[149]
$KTaO_3$ and NiOx/$KTaO_3$	Hydrothermal method followed by impregnation method	Reduction of CO_2 to methanol in isopropanol	UV light (250 W high-pressure mercury lamp; λ = 365 nm)	[150]
$NaNbO_3$ and $NaTaO_3$	Solid-state reaction	Reduction of CO_2 to $CO/H_2/CH_3OH/CH_4$ (CO was the major product)	UV light (four UV fluorescent lamps of 6 W; λ = 365 nm)	[152]
BiOI/$NaNbO_3$ p–n junction	Chemical bath method	Methylene blue (MB)	Visible light (500 W Xe lamp)	[154]
Ru/$NaNbO_3$ nanocomposite	Solvothermal method followed by photo-deposition technique	rhodamine (RhB)	Visible light (500 W Xe arc lamp (420 nm < λ < 800 nm)	[155]
Cubic phase $NaNbO_3$	Surface ligand-assisted localized crystallization (SLALC) method	Methylene blue (MB)	UV to Visible (100 W Hg arc lamp; λ = 365–600 nm)	[156]
Pt/$NaNbO_3$	Hydrothermal method combined with the photo-deposition	H_2 production by water/methanol mixture and degradation of rhodamine B (RhB) and 4-chlorophenol (CP)	Mimic sunlight irradiation and visible light (300 W Xe arc lamp)	[157]
Single-crystalline $NaNbO_3$	Hydrothermal treatment	Water splitting of H_2	300 W Xe arc lamp	[158]
g–C_3N_4/$NaNbO_3$	Ultrasonic dispersion followed by heat treatment method	Reduction of CO_2 to CH_4	300 W Xe arc lamp	[161]
Bi-doped $KNbO_3$	Solid-state reaction	Methyl orange (MO)	UV light (λ = 254 nm)	[162]

5 Conclusions and Insights

Perovskite oxides with the composition ABO_3 offer ample scope in designing novel compounds by the partial substitution of metal cations in A- and B-sites, which allows the preparation of isostructural series with different physical/chemical properties. The arrangement and position of the metal ions should be taken into consideration to understand the physical properties of perovskites. From the photocatalytic point of view, these perovskite materials have a special structural feature that is beneficial to photocatalytic activity. The relationship between crystal structure and energy delocalization shows that the closer to 180° the B–O–B bond angle is, the easier the excitation energy is delocalized leading to higher photoactivity. Thus, the bond angle between metal–oxygen–metal (B–O–B) in perovskite oxide is a significant structural parameter and must be taken into account. The modification of the electronic structure of a perovskite by dopants into its lattice is an effective way to affect its photocatalytic properties. However, more efforts needed to clarify the relationship between electronic structure and photocatalytic activity to develop novel perovskites with efficient photocatalytic activity. Other than band gap energy, crystallite size, and surface area, the vacancy of a metal cation and O^{2-} anions play important roles in the photocatalytic performance of perovskites oxides. The selection of preparative method also plays a significant role in the photocatalytic performance. A traditional method like high-temperature solid-state reaction results in the destruction of pore structures, and hence too low surface areas. Hence, controlled preparation of porous perovskite materials with a high surface area is highly desirable. The strategies as discussed are widely used to enhance the photocatalytic performance of perovskites. But the literature available on the adverse effect of such methods is limited. This should be considered appropriately in future.

Acknowledgements Authors would like to acknowledge CSIR, New Delhi under the CSIR-scheme (No. 01(2857)/16/EMR-II) for their financial support. PV thanks University Grants Commission (UGC)-Dr. D. S. Kothari Postdoctoral Fellowship (DSKPDF) Scheme, New Delhi for his postdoctoral research fellowship. MV thanks UGC New Delhi for the award of BSR fellowship.

References

1. Rao AN, Sivasankar B, Sadasivam V (2009) Kinetic studies on the photocatalytic degradation of Direct Yellow 12 in the presence of ZnO catalyst. J Mol Catal A Chem 306:77–81
2. Rauf MA, Ashraf SS (2009) Radiation induced degradation of dyes—an overview. J Hazard Mater 166:6–16
3. Akyol A, Bayramoglu M (2008) The degradation of an azo dye in a batch slurry photocatalytic reactor. Chem Eng Process 47:2150–2156

4. Ohtani B (2010) Photocatalysis A to Z—what we know and what we do not know in a scientific sense. J Photochem Photobiol C 11:157–178
5. Bahnemann D (2004) Photocatalytic water treatment: solar energy applications. Sol Energy 77:445–459
6. Zhang D, Li G, Li H et al (2013) The development of better photocatalysts through composition- and structure-engineering. Chem Asian J 8:26–40
7. Ch Samuel H S, Ta YW, Ch Juan J (2011) Recent developments of metal oxide semiconductors as photocatalysts in advanced oxidation processes (AOPs) for treatment of dye waste-water. J Chem Technol Biotechnol 86:1130–1158
8. Marye AF, Maria TD (1995) Heterogeneous photocatalysis. Chem Rev 83:341–357
9. Rauf MA, Ashraf SS (2009) Fundamental principles and application of heterogeneous photocatalytic degradation of dyes in solution. Chem Eng J 151:10–18
10. Krishnan R, Abegayl T, Csaba J (2015) Photocatalytic activity of inorganic semiconductor surfaces: myths, hype, and reality. J Phys Chem Lett 6:139–147
11. Fujishima A, Honda K (1972) Electrochemical photolysis of water at a semiconductor electrode. Nature 238:37–38
12. Chen X, Shen S, Guo L et al (2010) Semiconductor-based photocatalytic hydrogen generation. Chem Rev 110:6503–6570
13. Chen X, Mao SS (2007) Titanium dioxide nanomaterials: synthesis, properties, modifications, and applications. Chem Rev 107:2891–2959
14. Ji PF, Takeuchi M, Cuong TM et al (2010) Recent advances in visible light-responsive titanium oxide-based photocatalysts. Res Chem Intermed 36:327–347
15. Kato H, Kudo A (2002) Visible-light-response and photocatalytic activities of TiO_2 and $SrTiO_3$ photocatalysts co-doped with Antimony and Chromium. J Phys Chem B 106:5029–5034
16. Liu JW, Chen G, Li ZH et al (2006) Electronic structure and visible light photocatalysis water splitting property of chromium-doped $SrTiO_3$. J Solid State Chem 179:3704–3708
17. Hwang DW, Kim HG, Lee JS et al (2005) Photocatalytic hydrogen production from water over M-Doped $La_2Ti_2O_7$ (M = Cr, Fe) under visible light irradiation ($\lambda > 420$ nm). J Phys Chem B 109:2093–2102
18. Asahi R, Morikawa T, Ohwaki T et al (2001) Visible-light photocatalysis in nitrogen-doped titanium oxides. Science 293:269–271
19. Zaleska A, Grabowska E, Sobczak JW et al (2009) Photocatalytic activity of boron-modified TiO_2 under visible light: The effect of boron content, calcination temperature and TiO_2 matrix. Appl Catal B 89:469475
20. Paven-Thivet CL, Ishikawa A, Ziani A et al (2009) Photoelectrochemical properties of crystalline perovskite lanthanum titanium oxynitride films under lisible light. J Phys Chem C 113:6156–6162
21. Lu D, Hitoki G, Katou E et al (2004) Porous single-crystalline TaON and Ta_3N_5 particles. Chem Mater 16:1603–1605
22. Yashima M, Lee Y, Domen K (2007) crystal structure and electron density of tantalum oxynitride, a visible light responsive photocatalyst. Chem Mater 19:588–593
23. Li X, Kikugawa N, Ye J (2008) Nitrogen-doped lamellar niobic acid with visible light-responsive photocatalytic activity. Adv Mater 20:3816–3819
24. Matsumoto Y, Koinuma M, Iwanaga Y et al (2009) N-doping of oxide nanosheets. J Am Chem Soc 131:6644–6645
25. Luo M, Lu P, Yao W et al (2016) Shape and composition effects on photocatalytic hydrogen production for Pt–Pd Alloy co-catalysts. ACS Appl Mater Interfaces 8:20667–20674
26. Qin J, Zeng H (2017) Photocatalysts fabricated by depositing plasmonic Ag nanoparticles on carbon quantum dots/graphitic carbon nitride for broad spectrum photocatalytic hydrogen generation. Appl Catal B 209:161–173
27. Rather RA, Singh S, Pal B (2017) A C_3N_4 surface passivated highly photoactive Au–TiO_2 tubular nanostructure for the efficient H_2 production from water under sunlight irradiation. Appl Catal B 213:9–17

28. Jiang Y, Guo S, Hao R et al (2016) A hybridized heterojunction structure between TiO_2 nanorods and exfoliated graphitic carbon-nitride sheets for hydrogen evolution under visible light. Cryst Eng Commun 18:6875–6880
29. Tay Q, Wang X, Zhao X et al (2016) Enhanced visible light hydrogen production via a multiple heterojunction structure with defect-engineered g–C_3N_4 and twophase anatase/brookite TiO_2. J Catal 342:55–62
30. Yu X, Li W, Li Z et al (2017) Defect engineered Ta_2O_5 nanorod: One-pot synthesis, visible-light driven hydrogen generation and mechanism. Appl Catal B 217:48–56
31. Hirakawa H, Hashimoto M, Shiraishi Y et al (2017) Selective nitrate-to-ammonia transformation on surface defects of titanium dioxide photocatalysts. ACS Catal 7:3713–3720
32. Chen P, Qin M, Chen Z et al (2016) Solution combustion synthesis of nanosized WOx: characterization, mechanism and excellent photocatalytic properties. RSC Adv 6:83101–83109
33. Bao N, Shen L, Takata T et al (2008) Self-templated synthesis of nanoporous CdS nanostructures for highly efficient photocatalytic hydrogen production under visible light. Chem Mater 20:110–117
34. Yan H, Yang J, Ma G et al (2009) Visible-light-driven hydrogen production with extremely high quantum efficiency on Pt–PdS/CdS photocatalyst. J Catal 266:165–168
35. Borgarello E, Kiwi J, Pelizzetti E et al (1981) Sustained water cleavage by visible light. J Am Chem Soc 103:6324–6329
36. Chen F, Deng Z, Li X et al (2005) Visible light detoxification by 2,9,16,23-tetracarboxyl phthalocyanine copper modified amorphous titania. Chem Phys Lett 415:85–88
37. Nguyen TV, Wu JCS, Chiou CH (2008) Photoreduction of CO_2 over Ruthenium dye-sensitized TiO_2-based catalysts under concentrated natural sunlight. Catal Commun 9:2073–2076
38. Tyagi M, Tomar M, Gupta V (2014) Fabrication of an efficient GLAD-assisted p–NiO nanorod/n–ZnO thin film heterojunction UV photodiode. J Mater Chem C 2:2387–2393
39. Schuster F, Laumer B, Zamani RR et al (2014) p–GaN/n–ZnO heterojunction nanowires: optoelectronic properties and the role of interface polarity. ACS Nano 8:4376–4384
40. Luan P, Xie MZ, Fu XD et al (2015) Improved photoactivity of TiO_2–Fe_2O_3 nanocomposites for visible-light water splitting after phosphate bridging and its mechanism. Phys Chem Chem Phys 17:5043–5050
41. Xie MZ, Fu XD, Jing LQ et al (2014) Long-lived, visible-light-excited charge carriers of TiO_2/$BiVO_4$ nanocomposites and their unexpected photoactivity for water splitting. Adv Energy Mater 4:1300995
42. Humayun M, Zada A, Li ZJ et al Enhanced visible-light activities of porous $BiFeO_3$ by coupling with nanocrystalline TiO_2 and mechanism. Appl Catal B 180:219–226
43. Yan W, Hou W, Wenguang T et al (2018) Quasi-polymeric construction of stable perovskite-type $LaFeO_3$/g–C_3N_4 heterostructured photocatalyst for improved Z-scheme photocatalytic activity via solid p-n heterojunction interfacial effect. J Hazard Mater 347:412–422
44. Tanaka H, Misono M (2001) Advances in designing perovskite catalysts. Curr Opin Solid State Mater Sci 5:381–387
45. Cheong SW, Mostovoy M (2007) Multiferroics: a magnetic twist for ferroelectricity. Nat Mater 6:13–20
46. Pickett WE, Singh DJ (1996) Electronic structure and half-metallic transport in the $La_{1-x}Ca_xMnO_3$ system. Phys Rev B 53:1146
47. Kobayashi KI, Kimura T, Sawada H et al (1998) Room-temperature magnetoresistance in an oxide material with an ordered double-perovskite structure. Nature 395:677–680
48. Cava RJ, Batlogg B, Krajewski JJ et al (1988) Superconductivity near 30 K without copper: the $Ba_{0.6}K_{0.4}BiO_3$ perovskite. Nature 332:814–816
49. Bhalla AS, Guo R, Roy R (2000) The perovskite structure–a review of its role in ceramic science and technology. Mater Res Innov 4:3–26

50. Huang YH, Dass RI, Xing ZL et al (2005) Double perovskites as anode materials for solid-oxide fuel cells. Science 312:254–257
51. Green MA, Ho-Baillie A, Snaith HJ (2014) The emergence of perovskite solar cells. Nat Photonics 8:506–514
52. Wiegel M, Emond MHJ, Stobbe ER et al (1994) Luminescence of alkali tantalates and niobates. J Phys Chem Solids 55:773–778
53. Kudo A, Kato H, Nakagawa S (2000) Water splitting into H_2 and O_2 on new $Sr_2M_2O_7$ (M = Nb and Ta) photocatalysts with layered perovskite structure: factors affecting the photocatalytic activity. J Phys Chem B 104:571–575
54. Ewelina G (2016) Selected perovskite oxides: characterization, preparation and photocatalytic properties—a review. Appl Catal B 186:97–126
55. Guan Z, Gang L, Lianzhou W et al (2016) Inorganic perovskite photocatalysts for solar energy utilization. Chem Soc Rev 45:5951–5984
56. Sheng Z, Piyush K, Ujwal Kumar T et al (2018) A Review on photocatalytic CO_2 reduction using perovskite oxide nanomaterials. Nanotechnology 29:052001
57. Pushkar K, Zhong Ch (2014) Review on visible light active perovskite-based photocatalysts. Molecules 19:19995–20022
58. Saumyaprava A, Satyabadi M, Prakash ChS et al (2015) Glimpses of the modification of perovskite with graphene-analogous materials in photocatalytic applications. Inorg Chem Front 2:807–823
59. Jinwen S, Liejin G (2012) ABO_3-based photocatalysts for water splitting. Prog Nat Sci Mater Int 22:592–615
60. Wei W, Moses OT, Zongping S (2015) Research progress of perovskite materials in photocatalysis- and photovoltaics-related energy conversion and environmental treatment. Chem Soc Rev 44:5371–5408
61. Zhu J, Li H, Zhong L et al (2014) Perovskite oxides: preparation, characterizations, and applications in heterogeneous catalysis. ACS Catal 4:2917–2940
62. Shi R, Waterhouse GIN, Tierui Z (2017) Recent progress in photocatalytic CO_2 reduction over perovskite oxides. Sol. RRL 1:1700126–1700143
63. Koferstein R, Jager L, Ebbinghaus SG (2013) Magnetic and optical investigations on $LaFeO_3$ powders with different particle sizes and corresponding ceramics. Solid State Ionics 249–250:1–5
64. Arima T, Tokura Y, Torrence JB (1993) Variation of optical gaps in perovskite-type 3d transition-metal oxides. Phys Rev B 48:17006–17009
65. Xu JJ, Wang ZL, Xu D et al (2014) 3D ordered macroporous $LaFeO_3$ as efficient electrocatalyst for Li–O_2 batteries with enhanced rate capability and cyclic performance. Energy Environ Sci 7:2213–2219
66. Jauhar S, Singhal S (2014) Chromium and copper substituted lanthanum nanoferrites: their synthesis, characterization and application studies. J Mol Struct 1075:534–541
67. Sivakumar M, Gedanken A, Zhong W et al (2004) Sonochemical synthesis of nanocrystalline $LaFeO_3$. J Mater Chem 14:764–769
68. Popa M, Moreno JMC (2011) Lanthanum ferrite ferromagnetic nanocrystallites by a polymeric precursor route. J Alloy Compd 509:4108–4116
69. Li S, Wang X (2015) Synthesis of different morphologies lanthanum ferrite ($LaFeO_3$) fibers via electrospinning. Optik 126:408–410
70. Thirumalairajan S, Girija K, Hebalkar NY et al (2013) Shape evolution of perovskite $LaFeO_3$ nanostructures: a systematic investigation of growth mechanism, properties and morphology dependent photocatalytic activities. RSC Adv 3:7549–7561
71. Thirumalairajan S, Girija K, Ganesh I et al (2012) Controlled synthesis of perovskite $LaFeO_3$ microsphere composed of nanoparticles via self-assembly process and their associated photocatalytic activity. Chem Eng J 209:420–428
72. Li FT, Liu Y, Liu RH et al (2010) Preparation of Ca-doped $LaFeO_3$ nanopowders in a reverse microemulsion and their visible light photocatalytic activity. Mater Lett 64:223–225

73. Dong S, Xu K, Tian G (2009) Photocatalytic activities of $LaFe_{1-x}Zn_xO_3$ nanocrystals prepared by sol–gel auto-combustion method. J Mater Sci 44:2548–2552
74. Hou L, Sun GF, Liu K et al (2006) Preparation, characterization and investigation of catalytic activity of Li-doped $LaFeO_3$ nanoparticles. J Sol–Gel Sci Technol 40:9–14
75. Wei ZX, Wang Y, Liu JP et al (2012) Synthesis, magnetization and photocatalytic activity of $LaFeO_3$ and $LaFe_{0.5}Mn_{0.5-x}O_{3-\delta}$. Mater Chem Phys 136:755–761
76. Natali Sora I, Caronna T, Fontana F et al (2012) Crystal structures and magnetic properties of strontium and copper doped lanthanum ferrites. J Solid State Chem 191:33–39
77. Parrino F, García-Lopez E, Marcìa G et al (2016) Cu-substituted lanthanum ferrite perovskites: preparation, characterization and photocatalytic activity in gas-solid regime under simulated solar light irradiation. J Alloy Compd 682:686–694
78. Jauhar S, Dhiman M, Bansal S et al (2015) Mn^{3+} ion in perovskite lattice: a potential Fenton's reagent exhibiting remarkably enhanced degradation of cationic and anionic dyes. J Sol Gel Sci Technol 75:124–133
79. Dhiman M, Tripathi M, Singhal S et al (2017), Structural, optical and photocatalytic properties of different metal ions (Cr^{3+}, Co^{2+}, Ni^{2+}, Cu^{2+} and Zn^{2+}) substituted quaternary perovskites. Mater Chem Phys 202:40–49
80. Xicai H, Yongcai Z (2017) Low temperature gel-combustion synthesis of porous nanostructure $LaFeO_3$ with enhanced visible-light photocatalytic activity in reduction of Cr(VI). Mater Lett 197:120–122
81. Giuseppina I, Vincenzo V, Diana S et al (2016) Photocatalytic conversion of glucose to H_2 over $LaFeO_3$ perovskite nanoparticles. Chem Eng Trans 47:283–288
82. Ren X, Yang HT, Gen S et al (2016) Controlled growth of $LaFeO_3$ nanoparticles on reduced graphene oxide for highly efficient photocatalysis. Nanoscale 8:752–756
83. Muhammad H, Ning S, Fazal R et al (2018) Synthesis of ZnO/Bi-doped porous $LaFeO_3$ nanocomposites as highly efficient nano-photocatalysts dependent on the enhanced utilization of visible-light-excited electrons. Appl Catal B 231:23–33
84. Ibrahim MN, Shaolong W, Liang L et al (2018) Facile preparation of n-Type $LaFeO_3$ perovskite film for efficient photoelectrochemical water splitting. ChemistrySelect 3:968–972
85. Hsish TH, Jhong FH, Roy DT et al (2012) Electrical properties of $(La_{0.9}Ca_{0.1})(Co_{1-x}Ni_x)O_{3-\delta}$ cathode materials for SOFCs. Ceram Int 38:1785–1791
86. Wang Y, Ren J, Wang Y et al (2008) Nanocasted synthesis of mesoporous $LaCoO_3$ perovskite with extremely high surface area and excellent activity in methane combustion. J Phys Chem C 112:15293–15298
87. Feng L, Okonkwo CA, Qiong X et al (2016) PdO/$LaCoO_3$ heterojunction photocatalysts for highly hydrogen production from formaldehyde aqueous solution under visible light. Int J Hydrogen Energy 41:6115–6122
88. Minghui W, Mingping L, Minxue G et al (2017) Sugarcane bagasse hydrolysis by metal ions mediated synthesis of perovskite $LaCoO_3$ and the photocatalytic performance for hydrogen from formaldehyde solution under visible light. ACS Sustainable Chem Eng 5:11558–11565
89. Malleshappa J, Nagabhushana H, Sharma SC et al (2015) Leucas aspera mediated multifunctional CeO_2 nanoparticles: structural, photoluminescent, photocatalytic and antibacterial properties. Spectrochim Acta Part A 149:452–462
90. Liqing W, Qi P, Qianqian S et al (2015) Novel microbial synthesis of Cu doped $LaCoO_3$ photocatalyst and its high efficient hydrogen production from formaldehyde solution under visible light irradiation. Fuel 140:267–274
91. Jayapandi S, Lakshmi D, Premkumar S et al (2018) Augmented photocatalytic and electrochemical activities of Ag tailored $LaCoO_3$ perovskite semiconductor. Mater Lett 218:205–208
92. Shaterian M, Enhessari M, Rabbani D et al (2014) Synthesis, characterization and photocatalytic activity of $LaMnO_3$ nanoparticles. Appl Surf Sci 318:213–217
93. Jie H, Jiahua M, Lina W et al (2014) Preparation, characterization and photocatalytic activity of co-doped $LaMnO_3$/graphene composites. Powder Technol 54:556–562

94. Mi Y, Zeng S, Li L et al (2012) Solvent directed fabrication of Bi_2WO_6 nanostructures with different morphologies: Synthesis and their shape-dependent photocatalytic properties. Mater Res Bull 47:2623–2630
95. Rajesh Kumar S, Abinaya CV, Amirthapandian S et al (2017) Enhanced visible light photocatalytic activity of porous $LaMnO_3$ sub-micron particles in the degradation of rose bengal. Mater Res Bull 93:270–281
96. Peisong T, Longlong Y, Jiayuan M et al (2017) Preparation of nanocrystalline $YbFeO_3$ by sol–gel method and its visible-light photocatalytic activities. Ferroelectrics 521:71–76
97. Peisong T, Chen H, Lv Chunyan et al (2017) Microwave synthesis of nanoparticulate $EuFeO_3$ and its visible light photocatalytic activity. Integr Ferroelectr 181:49–54
98. Yupeng Y, Xueliang Z, Lifei L et al (2008) Synthesis and photocatalytic characterization of a new photocatalyst $BaZrO_3$. Int J Hydrogen Energy 33:5941–5946
99. Yupeng Y, Zongyan Z, Jing Z et al (2010) Polymerizable complex synthesis of $BaZr_{1-x}Sn_xO_3$ photocatalysts: Role of Sn^{4+} in the band structure and their photocatalytic water splitting activities. J Mater Chem 20:6772–6779
100. Yupeng Y, Lv J, Jiang XJ et al (2007) Large impact of strontium substitution on photocatalytic water splitting activity of $BaSnO_3$. Appl Phys Lett 91:094107
101. Borse PH, Joshi UA, Ji SM et al (2007) Band gap tuning of lead-substituted $BaSnO_3$ for visible light photocatalysis. Appl Phys Lett 90:034103
102. Borja-Urby R, Díaz-Torres LA, Salas P et al (2011) Structural study, photoluminescence, and photocatalytic activity of semiconducting BaZrO3: Bi nanocrystals. J Mater Sci Eng B 176:1382–1387
103. Ziyauddin K, Mohammad Q (2012) Tantalum doped $BaZrO_3$ for efficient photocatalytic hydrogen generation by water splitting. Catal Commun 28:82–85
104. Kazuhiko M, Kazunari D (2012) Water oxidation using a particulate $BaZrO_3$–$BaTaO_2N$ solid-solution photocatalyst that operates under a wide range of visible light. Angew Chem Int Ed 51:9865–9869
105. Magdalena M, Beata B, Paweł M et al (2017) Preparation and photocatalytic properties of $BaZrO_3$ and $SrZrO_3$ modified with Cu_2O/Bi_2O_3 quantum dots. Solid State Sci 74:13–23
106. Alammar T, Hamm I, Wark M, Mudring A-V et al (2015) Low-temperature route to metal titanate perovskite nanoparticles for photocatalytic applications. Appl Catal B 178:20–28
107. Zhu S, Salvador PA, Rohrer GS et al (2017) Controlling the termination and photochemical reactivity of the $SrTiO_3$ (110) surface. Phys Chem Chem Phys 19:7910–7918
108. da Silva LF, Lopes OF, de Mendonca VR, Carvalho KTG, Longo E, Ribeiro C, Mastelaro VR et al (2016) An understanding of the photocatalytic properties and pollutant degradation mechanism of $SrTiO_3$ nanoparticles. Photochem Photobiol 9:371–378
109. Xian T, Di L, Sun X, Ma J, Zhou Y, Wei X et al (2018) Photocatalytic degradation of dyes over Au decorated $SrTiO_3$ nanoparticles under simulated sunlight and visible light irradiation. J Ceram Soc Jpn 126:354–359
110. Liu X, Jiang J, Jia Y, Qiu J, Xia T, Zhang Y, Li Y, Chen X et al (2017) Insight into synergistically enhanced adsorption and visible light photocatalytic performance of Z-scheme heterojunction of SrTiO3(La, Cr)-decorated WO_3 nanosheets. Appl Surf Sci 412:279–289
111. Kiss B, Manning TD, Hesp D et al (2017) Nano-structured rhodium doped $SrTiO_3$-Visible light activated photocatalyst for water decontamination. Appl Catal B 206:547–555
112. Devi LG, Anitha BG (2018) Exploration of vectorial charge transfer mechanism in TiO_2/$SrTiO_3$ composite under UV light illumination for the degradation of 4-Nitrophenol: a comparative study with TiO_2 and $SrTiO_3$. Surf Interfaces 11:48–56
113. Challagulla S, Nagarjuna R, Roy S et al (2017) Scalable free-radical polymerization based sol–gel synthesis of $SrTiO_3$ and its photocatalytic activity. ChemistrySelect 2:4836–4842
114. Goto Y, Hisatomi T, Wang Q et al (2018) A particulate photocatalyst water-splitting panel for large-scale solar hydrogen generation. Joule 2:509–520
115. Saadetnejad D, Yıldırım R (2018) Photocatalytic hydrogen production by water splitting over Au/Al–$SrTiO_3$. Int J Hydrogen Energy 43:1116–1122

116. Han K, Lin YC, Yang CM et al (2017) Promoting photocatalytic overall water splitting by controlled magnesium incorporation in $SrTiO_3$ photocatalysts. Chem Sus Chem 10:4510–4516
117. Kou J, Gao J, Li Z et al (2015) Construction of visible-light-responsive $SrTiO_3$ with enhanced CO_2 adsorption ability: highly efficient photocatalysts for artifical photosynthesis. Catal Lett 145:640–646
118. Luo C, Zhao J, Li Y et al (2018) Photocatalytic CO_2 reduction over $SrTiO_3$: correlation between surface structure and activity. Appl Surf Sci 447:627–635
119. Li D, Ouyang S, Xu H et al (2016) Synergistic effect of Au and Rh on $SrTiO_3$ in significantly promoting visible-light-driven syngas production from CO_2 and H_2O. Chem Commun 52:5989–5992
120. Shoji S, Yin G, Nishikawa M et al (2016) Photocatalytic reduction of CO_2 by Cu_xO nanocluster loaded $SrTiO_3$ nanorod thin film. Chem Phys Lett 658:309–314
121. Pan JH, Cai ZC, Yu Y, Zhao XS (2011) Controllable synthesis of mesoporous F–TiO_2 spheres for effective photocatalysis. J Mater Chem 21:11430–11438
122. Yang D, Sun YY, Tong ZW, Nan YH, Jiang ZY (2016) Fabrication of bimodal-pore $SrTiO_3$ microspheres with excellent photocatalytic performance for Cr(VI) reduction under simulated sunlight. J Hazard Mater 312:45–54
123. Dong Y, Xiaoyan Z, Yuanyuan S, Zhenwei T, Zhongyi J (2018) Fabrication of three-dimensional porous La-doped $SrTiO_3$ microspheres with enhanced visible light catalytic activity for Cr(VI) reduction. Front Chem Sci Eng 12:440–449
124. Cheng Z, Lin J (2010) Layered organic–inorganic hybrid perovskites: structure, optical properties, film preparation, patterning and templating engineering. Cryst Eng Commun 12:2646–2662
125. Yan Y, Yang H, Zhao X et al (2018) Enhanced photocatalytic activity of surface disorder-engineered $CaTiO_3$. Mater Res Bull 105:286–290
126. Kumar A, Schuerings C, Kumar S et al (2018) Perovskite-structured $CaTiO_3$ coupled with g–C_3N_4 as a heterojunction photocatalyst for organic pollutant degradation. Beilstein J Nanotechnol 9:671–685
127. Yan Y, Yang H, Zhao X et al (2018) A Hydrothermal route to the synthesis of $CaTiO_3$ nanocuboids using P25 as the titanium source. J Electron Mater 47:3045–3050
128. Han C, Liu J, Yang W et al (2017) Photocatalytic activity of $CaTiO_3$ synthesized by solid state, sol–gel and hydrothermal methods. J Sol–Gel Sci Technol 81:806–813
129. Zhang H, Chen G, He X et al (2012) Electronic structure and photocatalytic properties of Ag–La codoped $CaTiO_3$. J Alloys Compd 516:91–95
130. Im Y, Park S-M, Kang M (2017) Effect of Ca/Ti Ratio on the core-shell structured $CaTiO_3$@basalt fiber for effective photoreduction of carbon dioxide. Bull Korean Chem Soc 38:397–400
131. Yoshida H, Zhang L, Sato M et al (2015) Calcium titanate photocatalyst prepared by a flux method for reduction of carbon dioxide with water. Catal Today 251:132–139
132. Selvarajan S, Malathy P, Suganthi A et al (2017) Fabrication of mesoporous $BaTiO_3/SnO_2$ nanorods with highly enhanced photocatalytic degradation of organic pollutants. J Ind Eng Chem 53:201–212
133. Nageri M, Kumar V (2018) Manganese-doped $BaTiO_3$ nanotube arrays for enhanced visible light photocatalytic applications. Mater Chem Phys 213:400–405
134. Thamima M, Andou Y, Karuppuchamy S (2017) Microwave assisted synthesis of perovskite structured $BaTiO_3$ nanospheres via peroxo route for photocatalytic applications. Ceram Int 43:556–563
135. Maeda K (2014) Rhodium-doped barium titanate perovskite as a stable p-type semiconductor photocatalyst for hydrogen evolution under visible light. ACS Appl Mater Interfaces 6:2167–2173
136. Yan SC, Wang JQ, Li ZS et al (2009) Photocatalytic activities for water splitting of La-doped $NaTaO_3$ fabricated by microwave synthesis. Solid State Ionics 180:1539–1542

137. Wang S, Xu X, Luo H et al (2016) Enhanced organic dye removal of the W and N co-doped $NaTaO_3$ under visible light irradiation. J Alloys Compd 681:225–232
138. Lan NT, Phan LG, Hoang LH et al (2016) Hydrothermal synthesis, structure and photocatalytic properties of La/Bi co-doped $NaTaO_3$. Mater Trans 57:1–4
139. Li FF, Liu DR, Gao GM et al (2015) Improved visible-light photocatalytic activity of $NaTaO_3$ with perovskite-like structure via sulfur anion doping. Appl Catal B 166–167:104–111
140. Kato H, Kudo A (1999) Highly efficient decomposition of pure water into H_2 and O_2 over $NaTaO_3$ photocatalysts. Catal Lett 58:153–155
141. Jana P, Montero CM, Pizarro P et al (2014) Photocatalytic hydrogen production in the water/methanol system using Pt/RE: $NaTaO_3$ (RE = Y, La, Ce, Yb) catalysts. Int J Hydrogen Energy 39:5283–5290
142. Lopez-Juarez R, Gonzalez F, Cipagauta S et al (2016) Solid state synthesis of La-doped $NaTaO_3$ under time-reduced conditions and its photocatalytic properties. Ceram Silikáty 60:278–284
143. Liu X, Lv J, Wang S et al (2015) A novel contractive effect of $KTaO_3$ nanocrystals via La^{3+} doping and an enhanced photocatalytic performance. J Alloys Compd 622:894–901
144. Krukowska A, Trykowski G, Winiarski MJ et al (2018) Mono- and bimetallic nanoparticles decorated $KTaO_3$ photocatalysts with improved Vis and UV–Vis light activity. Appl Surf Sci 441:993–1011
145. Bajorowicz B, Reszczyńska J, Lisowski W et al (2015) Perovskite-type $KTaO_3$-reduced graphene oxide hybrid with improved visible light photocatalytic activity. RSC Adv 5:91315–91325
146. Chen Z, Xing P, Chen P et al (2018) Synthesis of carbon doped $KTaO_3$ and its enhanced performance in photocatalytic H_2 generation. Catal Commun 109:6–9
147. Xiang T, Xin F, Zhao C et al (2018) Fabrication of nano copper oxide evenly patched on cubic sodium tantalate for oriented photocatalytic reduction of carbon dioxide. J Colloid Interface Sci 518:34–40
148. Nakanishi H, Iizuka K, Takayama T et al (2017) Highly active $NaTaO_3$-based photocatalysts for CO_2 reduction to form CO using water as the electron donor. Chem Sus Chem 10:112–118
149. Shao X, Yin X, Wang J (2018) Nanoheterostructures of potassium tantalate and nickel oxide for photocatalytic reduction of carbon dioxide to methanol in isopropanol. J Colloid Interface Sci 512:466–473
150. Li K, Handoko AD, Khraisheh M et al (2014) Photocatalytic reduction of CO_2 and protons using water as an electron donor over potassium tantalate nanoflakes. Nanoscale 6:9767–9773
151. Fresno F, Jana P, Renones P et al (2017) CO_2 reduction over $NaNbO_3$ and $NaTaO_3$ perovskite photocatalysts. Photochem Photobiol Sci 16:17–23
152. Wu W, Liang S, Chen Y et al (2013) Mechanism and improvement of the visible light photocatalysis of organic pollutants over microcrystalline $AgNbO_3$ prepared by a sol–gel method. Mater Res Bull 48:1618–1626
153. Sun M, Yan Q, Shao Y et al (2017) Facile fabrication of BiOI decorated $NaNbO_3$ cubes: A p-n junction photocatalyst with improved visible-light activity. Appl Surf Sci 416:288–295
154. Chen W, Hu Y, Ba M (2018) Surface interaction between cubic phase $NaNbO_3$ nanoflowers and Ru nanoparticles for enhancing visible-light driven photosensitized photocatalysis. Appl Surf Sci 435:483–493
155. Wang L, Gu H, He J et al (2017) Scale synthesized cubic $NaNbO_3$ nanoparticles with recoverable adsorption and photodegradation for prompt removal of methylene blue. J Alloys Compd 695:599–606
156. Liu Q, Chai Y, Zhang L et al (2017) Highly efficient Pt/$NaNbO_3$ nanowire photocatalyst: its morphology effect and application in water purification and H_2 production. Appl Catal B 205:505–513

157. Liu Q, Zhang L, Chai Y et al (2017) Facile fabrication and mechanism of single-crystal sodium niobate photocatalyst: insight into the structure features influence on photocatalytic performance for H_2 evolution. J Phys Chem C 121:25898–25907
158. Li P, Xu H, Liu L et al (2014) Constructing cubic–orthorhombic surface-phase junctions of $NaNbO_3$ towards significant enhancement of CO_2 photoreduction. J Mater Chem A 2:5606–5609
159. Shi H, Chen G, Zhang C et al (2014) Polymeric g–C_3N_4 coupled with $NaNbO_3$ nanowires toward enhanced photocatalytic reduction of CO_2 into renewable fuel. ACS Catal 4:3637–3643
160. Shi H, Zhang C, Zhou C et al (2015) Conversion of CO_2 into renewable fuel over Pt–g–C_3N_4/$KNbO_3$ composite photocatalyst. RSC Adv 5:93615–93622
161. Raja S, Babu RR, Ramamurthi K et al (2018) Magnetic and photocatalytic properties of bismuth doped $KNbO_3$ microrods. Mater Res Bull 105:349–359
162. Zhang T, Zhao K, Yu J et al (2013) Photocatalytic water splitting for hydrogen generation on cubic, orthorhombic, and tetragonal $KNbO_3$ microcubes. Nanoscale 5:8375–8383
163. Wang R, Zhu Y, Qiu Y et al (2013) Synthesis of nitrogen-doped $KNbO_3$ nanocubes with high photocatalytic activity for water splitting and degradation of organic pollutants under visible light. Chem Eng J 226:123–130
164. Hong Z, Li X, Kang SZ et al (2014) Enhanced photocatalytic activity and stability of the reduced graphene oxide loaded potassium niobate microspheres for hydrogen production from water reduction. Int J Hydrogen Energy 39:12515–12523